applied sciences

MDPI

Article

Antibacterial and In Vitro Bioactivity Studies of Silver-Doped, Cerium-Doped, and Silver–Cerium Co-Doped 80S Mesoporous Bioactive Glass Particles via Spray Pyrolysis

Mannie Belay Taye, Henni Setia Ningsih and Shao-Ju Shih *

Department of Materials Science and Engineering, National Taiwan University of Science and Technology, No. 43, Sec. 4, Keelung Road, Taipei City 10607, Taiwan; d10904812@mail.ntust.edu.tw (M.B.T.); hennisetianingsih@gmail.com (H.S.N.)

* Correspondence: shao-ju.shih@mail.ntust.edu.tw; Tel.: +886-2-27303716

Abstract: Researchers are concentrating on discovering reducing treatments for bacterial infections due to the worrisome and quick rise of drug-resistant microbial-related illnesses. Metallic ion doping and co-doping mesoporous bioactive glass (MBG) can defend against drug-resistant pathogens of *Escherichia coli* (*E. coli*) infection of wounds and solve the issues of bone deformities. In this study, un-doped MBG, silver-doped MBG (Ag-doped MBG), cerium-doped MBG (Ce-doped MBG), and silver–cerium co-doped MBG (Ag-Ce co-doped MBG) have been successfully synthesized via the spray pyrolysis method. In addition, various characterization techniques, including X-ray diffraction, field emission scanning electron microscopy, energy-dispersive X-ray spectroscopy, transmission electron microscopy, Fourier transform infrared spectroscopy, and nitrogen adsorption–desorption, were used to investigate the phase compositions, surface morphologies, chemical compositions, inner structure morphologies, chemical bonds/functional groups, and specific surface areas, respectively. The antibacterial efficacy against *E. coli* was assessed using the colony count technique. All types of MBG with Ag, Ce, and Ag-Ce were effective against *E. coli*. Furthermore, when immersed in simulated body fluid, the MBGs formed hydroxyapatite and could be used to improve bone defects. Only 5.75 mol% Ag-doped MBG showed toxicity in the MTT assay test. According to our analysis, the 80S-Ag-Ce-MBG was the first Ag-Ce co-doped MBG.

Keywords: silver; cerium; bioactive glass; spray pyrolysis

Citation: Taye, M.B.; Ningsih, H.S.; Shih, S.-J. Antibacterial and In Vitro Bioactivity Studies of Silver-Doped, Cerium-Doped, and Silver–Cerium Co-Doped 80S Mesoporous Bioactive Glass Particles via Spray Pyrolysis. *Appl. Sci.* **2023**, *13*, 12637. https://doi.org/10.3390/app132312637

Academic Editors: Tomasz Pikula and Agata Lisińska-Czekaj

Received: 5 October 2023
Revised: 17 November 2023
Accepted: 22 November 2023
Published: 24 November 2023

1. Introduction

In 2004, Zhao's team and Vallet Regi's group conducted experiments leading to the creation of a novel type of bioactive glass known as mesoporous bioactive glass (MBG) [1]. MBG is derived from the SiO_2–CaO–P_2O_5 system and features a well-ordered porosity with uniformly sized pores ranging from 2 to 50 nm. Specifically, the 80S ($80SiO_2$-16CaO-$4P_2O_5$) MBG composition offers numerous advantages, including heightened biocompatibility, osteoconductivity, and the controlled release of calcium and phosphate ions, which are essential for bone mineralization and regeneration. In addition, its mesoporous structure provides an extensive surface area and facilitates efficient ion exchange, bioactivity, and cell adhesion for bone growth [2,3]. These characteristics make it a favored choice for applications in bone tissue engineering and regeneration, aligning it closely with the natural bone environment and contributing to favorable outcomes in bone healing and reconstruction procedures [4]. In recent years, various metal ions, including silver, cerium, copper, gallium, and zinc, have emerged as therapeutic agents that can stimulate bone growth, angiogenesis, and antibacterial effects [5–7]. However, these metal ions have limitations, such as unstable ionic states and potential toxicity when directly consumed [8]. To address these challenges, substrates like zeolites, hydroxyapatite (HA), bioglass, silica, and carbon fibers have been employed to harness their antibacterial properties. To improve

the stability of ionic states and enable a gradual, sustained release of metal ions over an extended duration, extensive research has concentrated on developing antibacterial drugs where metal ions are bound to a substrate [8].

Drug-resistant infections pose a significant global health threat, an examination of their burden and treatment challenges. The emergence and spread of antimicrobial resistance (AMR) have escalated to a critical level, with estimates indicating that by 2050, AMR could lead to 10 million deaths annually worldwide, surpassing current mortality rates from cancer or road traffic accidents [9,10]. Factors contributing to this trend include overuse and misuse of antibiotics, inadequate infection control practices [11], and a lack of new antimicrobial agents [12]. Additionally, the economic impact of these infections is significant, with potential direct healthcare costs of up to USD 2.9 trillion and a projected loss of USD 100 trillion in global economic output by 2050 [13,14]. Therefore, understanding the burden of drug-resistant infections and their treatment challenges is crucial for developing effective interventions and policies. The alarming and rapid growth in drug-resistant microbial-related illnesses has motivated researchers to focus their attention on developing innovative therapies for bacterial infections [15]. Notably, *Staphylococcus aureus* (*S. aureus*), a Gram-positive bacterium, frequently colonizes both human skin and mucosal surfaces. The capacity of the bacterium to induce post-surgical and wound infections can be attributed to an array of virulence factors, such as adhesins, toxins, and mechanisms for immune evasion [16]. *E. coli*, on the other hand, has emerged as one of the most severe and drug-resistant infections globally [17,18], giving rise to various ailments such as post-surgical infections, wound infections, sepsis, urinary tract infections, sexually transmitted infections, and specific forms of diarrhea [19]. Consequently, drug-resistant infections are now recognized as severe concerns that can lead to a multitude of repercussions, including prolonged hospital stays, increased readmission rates, elevated pharmaceutical expenditures, lost workdays, post-discharge care, and even fatalities, as reported by the World Health Organization [1,18,20]. Researchers have turned to noble metallic ion-doped and co-doped mesoporous bioactive glass (MBG) to combat medication-resistant illnesses, particularly against bacteria like *E. coli* [21]. Among these ions, silver has the strongest antibacterial properties of any heavy metal used in this area [1]. MBG containing silver is an effective and broad-spectrum antibacterial ion that is more efficient against Gram-negative (*E. coli*) bacteria than Gram-positive (*S. aureus*) bacteria [1,22]. The several ways through which silver exerts its antibacterial effect are outlined here. The S-Ag bond is formed when Ag^+ ions interact with the surface proteins of bacterial cell walls' disulfide (S-S) and sulfhydryl (-SH) groups. These binding halts electron transport and respiration in addition to causing the collapse of the proton motive force in bacteria. As a result, it is more difficult to induce effective rescue mechanisms and the membrane is de-energized then the bacterial cell death based on these situations [23]. As a hypothesis, the most essential part of silver's antibacterial activity is the interaction between Ag^+ ions and thiol groups. This interaction disrupts the conformation of the thiol groups of cysteine residues, which are necessary for the activity of many enzymes, and so inactivates bacterial enzymatic activities [24,25], and cerium is a rare earth element that has been employed in biomaterials to enhance antibacterial activity [26]. Ce^{3+}-doped particles had an unusually significant antibacterial impact on *E. coli* [27], and co-doped MBG over the antibacterial activity of silver and cerium has been explained via a variety of processes and are practically related to the presence of Ag^+ and Ce^{3+} [28]. Further, previous studies have also described that Ag^+ and Ce^{3+} ions quickly bind to *E. coli* bacteria and enter the cytoplasm through the external and internal membranes, and alter their oxidation states (Ag^+, Ce^{3+}, and Ce^{4+}) [29], reducing reactive oxygen species (There are some reactive oxygen species (ROS) produced: $O_2^{\bullet -}$, H_2O_2, OH^-, and $^{\bullet}OH$). As a result, the bacteria's ability to breathe is impaired, and its RNA, DNA, protein, and lipids are damaged. The bacteria's cells are eventually dead [1], and high ROS exhibit favorable bioactivity and suitable cell contacts [26,30].

Silver and cerium-doped MBG are utilized for bone abnormalities in addition to antibacterial properties. A bone defect is the lack of bone tissue at a particular anatomical

site and is caused by an infection/revision surgery, a traumatic impact of great severity, or the removal of a tumor [31,32]. Severe bone defects can cause disability, restrict a person's capacity to live and work and place heavy social and financial constraints on them. The repair of bone defects is one of the most popular regenerative techniques; approximately one million cases of bone diseases and abnormalities are reported each year [33], yet more than 200,000 bone transplants are carried out globally each year [32]. Cerium has been shown to increase the proliferation, mineralization, and differentiation of primary osteoblasts, which can be employed for osteogenesis and angiogenesis. In addition, cerium plays a vital role in the process of bone healing surgery, while silver protects against infection at the surgical site. This is due to the ability of cerium to stimulate bone regeneration and silver's antimicrobial characteristics, both of which are integral components in ensuring favorable outcomes of surgical procedures [34,35]. Calcium phosphate (CP), which is the inherent form of calcium apatite, comprises the primary mineral constituent of bone fillers [36]. The utilization of calcium phosphate in MBG for bone restoration is driven by the crucial role played by calcium and phosphate ions in bone mineralization and regeneration. Substances like hydroxyapatite (HA), a variation of calcium phosphate, closely resemble the composition of natural bone, rendering them highly compatible with living tissues and conducive to the promotion of bone growth. When incorporated into MBG, CP enhances its resemblance to natural bone, facilitating the controlled release of these ions and establishing an environment that supports the activity of bone cells and the formation of bone-like apatite. Throughout our experimental phase, HA has exhibited a range of favorable attributes, including compatibility with living tissues, absence of toxicity, ability to support bone growth, lack of immunogenicity, and serving as a fundamental component in the process of bone formation [37,38]. Furthermore, cell viability (MTT assay), and in vitro bioactivity were addressed in-depth to determine the optimum nanoparticle related to low cytotoxicity and enhancing the filling of the bone defects for these materials.

In the realm of the prior investigation regarding the production of silver and cerium doped MBG with three main techniques were considered: melt-derived methods [39], sol-gel synthesis [40], and spray pyrolysis [41]. The melt-derived method offers a straightforward approach, expedited processing, and meticulous control over the glass composition. However, they pose certain challenges, such as maintaining the required high level of purity for optimal bioactivity and the potential introduction of impurities during various processing stages like polishing, grinding, sieving, and fritting [42]. In addition, the melt-derived method requires high temperatures, which increases production costs. On the other hand, sol-gel offers meticulous regulation over composition and structure but is time-consuming, intricate, and involves multiple stages of processing [43]. In order to solve the challenges mentioned earlier, the investigation utilizes the spray pyrolysis method, which distinguishes itself by offering a continuous, cost-effective, and safe approach. This method ensures the maintenance of high purity and facilitates low-temperature processing for bioactive glasses [44,45]. Its distinct advantage lies in the direct control over morphology, which is particularly crucial for mesoporous materials while also reducing exposure to hazardous substances [46]. For example, our previous research examined a comparison between the surface area and bioactivity of particles generated through spray pyrolysis (SP) and sol-gel techniques employing the same chemical composition [47]. The findings revealed that although the SP particles exhibited a smaller surface area, they displayed superior bioactivity with larger HA crystal sizes. This can be attributed to the rapid cooling in SP, which encourages the presence of metastable siloxanes, thereby increasing the number of nucleation sites for HA layers and consequently enhancing bioactivity [47,48]. Hence, the SP approach was utilized to manufacture mesoporous bioactive glass particles for this study.

Moreover, the introduction of a non-ionic tri-block copolymer surfactant of Pluronic F-127 EO106PO70EO106 (where EO is polyethylene oxide and PO is polypropylene oxide) to induce the synthesis of an ordered mesoporous glass with the highest pore volume and specific surface area (a surfactant concentration that offers a high ordered mesopore

while preventing the production of aggregated surfactant lamellae), and uniform and narrow pore size distribution [47,49]. Furthermore, the use of surfactants confers several advantages, including non-toxicity, biodegradability, fostering high bioactivity in the glass, influencing particle morphology, and offering a cost-effective solution. Additionally, surfactants contribute to interfacial stability and provide the capability to fine-tune characteristics based on molecular nucleation [50,51].

2. Materials and Methods

2.1. Synthesis

All MBG samples, including un-doped, silver-doped, cerium-doped, and silver–cerium co-doped MBG powders on the composition of $80SiO_2$-$16CaO$-$4P_2O_5$, were fabricated using SP with horizontal furnace, and a schematic diagram of SP system is shown in Figure 1. Firstly, to prepare an un-doped MBG solution, 4.35 g of calcium nitrate tetrahydrate ($Ca(NO_3)_2{\cdot}4H_2O$), 98 wt.%, Showa, Tokyo, Japan), 19.23 g of tetraethyl orthosilicate ($Si(OC_2H_5)_4$, ≥99 wt.%, Aldrich, Schnelldorf, Germany), 1.68 g of triethyl phosphate ($(C_2H_5)_3PO_4$, 98 wt.%, Alfa Aesar, Ward Hill, MA, USA), and 21.0 g of Pluronic F-127 $EO_{106}Po_{70}EO_{106}$ were dissolved into 120 mL ethanol (C_2H_5OH, 99.5%, Echo, Tainan, Taiwan). Then, 3 mL of 0.5 M hydrochloric acid (HCl, 37 wt.%, Honeywell, Charlotte, NC, USA) was added to the precursor solution and stirred for 12 h at room temperature using a magnetic stirrer to ensure solution homogeneity. The precursor solution was poured gently into 1080 mL of deionized water and stirred again for 1 h at room temperature. To prepare the doped MBG, 0.59 g of silver nitrate ($AgNO_3$, 99%, Echo, Taiwan) was used for 2.87 mol% Ag-doped MBG and 1.18 g for 5.75 mol% Ag-doped MBG. For cerium nitrate ($Ce(NO_3)_3{\cdot}6H_2O$, 99.5%, Alfa Aesar, Heysham, UK), 1.51 g was used for 2.87 mol% Ce-doped MBG, and 3.02 g for 5.75 mol% Ce-doped MBG. As for the preparation of 2.87 mol% Ag/2.87 mol% Ce co-doped MBG, 0.59 g of $AgNO_3$ and 1.51 g of $Ce(NO_3)_3{\cdot}6H_2O$ were mixed into 1080 mL of deionized water and stirred for an hour at room temperature then poured into the precursor solution and stirred for 1 h to synthesize Ag-doped or Ce-doped MBG. Finally, for the preparation of the co-doped MBG, cerium nitrate and silver nitrate were sequentially introduced into 1080 mL of deionized (DI) water with an interval of 1 h between each addition. Subsequently, the co-doped solution was poured into the precursor solution and stirred for an additional hour.

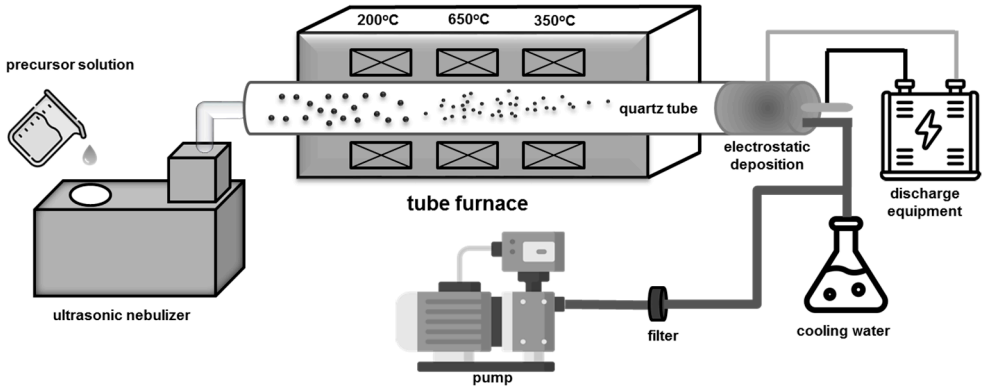

Figure 1. Schematic diagram of spray pyrolysis.

Next, for the SP process, the prepared MBG solutions were atomized using an ultrasonic nebulizer (King Ultrasonic Co., New Taipei City, Taiwan) with a frequency of 1.65 MHz. Subsequently, the droplets were transported into a quartz tube furnace (D110, Dengyng, New Taipei City, Taiwan) with preheating, calcination, and cooling zones at 400, 700, and 500 °C, respectively. Finally, the resulting MBG powders were collected from the steel tube [52,53] and dried at 70 °C for 24 h in the oven.

2.2. Characterization

Briefly, the phase composition of all MBG samples was determined using an X-ray diffractometer (D2 phaser, Bruker, Karlsruhe, Germany) with Cu Kα (λ = 0.154 nm) radiation at 30 kV and the current at 10 mA. The XRD samples were prepared by loading a small amount of MBG powders onto a 25 mm zero-background holder. The scanning angle (2θ) was set in the range of 20~80° with the scanning rate at 4°/min. FE-SEM (JSM-6500F, JEOL, Tokyo, Japan) mainly uses a focused electron beam to identify the sample surface morphology and microstructure. Energy-dispersive spectroscopy (EDS) analysis was used to describe the material compositions by using INCA software 7582-M (Oxford Instrument, Abingdon, UK). The MBG powders were fixed onto an SEM stub using double-sided carbon-conductive tape. The samples were then sputtered using platinum with a deposition rate of 30 s. The adsorption/desorption Isotherm (Novatouch LX2, Quantachrome, Boynton Beach, FL, USA) measurement method was proposed by Brunauer–Emmett–Teller (BET), which is determined via the physical adsorption of nitrogen gas on the pores/surface of the particles and Barrett–Joyner–Halenda (BJH) also measured pore size and pore volume. Nitrogen gas was used because it is abundant, inert, and high in purity. The microstructure of the un-doped, Ag-doped, Ce-doped, and Ag-Ce co-doped MBG were analyzed via TEM (Tecnai G2 F20, FEI, Hillsboro, OR, USA). For the preparation of the TEM sample, MBG powders were dispersed into an acetone solution using ultrasonic vibration for 10 min. Then, the dispersion was dropped on the surface of 300-mesh copper-coated TEM grids. Lastly, the principal hydroxyl apatite of the functional groups and structural bands in the dried MBG powders were assessed using Fourier-transform infrared spectroscopy (FTIR) (Thermo Nicolet AVATAR 370, Thermofisher, Waltham, MA, USA) in the wave number range from 400 to 4000 cm^{-1}.

2.3. Antibacterial Activity

The colony count was a technique used to conduct the antibacterial test, and all samples were tested for *E. coli* bacteria (DH5-Alpha, BCRC 51731, Hsinchu, Taiwan). The colony count method is a quantitative method that counts visible bacteria colonies on a culture medium to estimate the initial bacteria population. The selection of *E. coli* bacteria is supported by practicality, standardization, and clinical significance. *E. coli* functions as a practical bacterial model, facilitating initial evaluations and enabling the evaluation of material biocompatibility, which includes the identification of potential risks associated with bone surgeries [54]. The *E. coli* suspension has a concentration of 0.5 mL with a dilution at 6×10^5 colony-forming unit (CFU)/10 mL of phosphate-buffered saline solution. The un-doped, doped, and co-doped MBG-containing powders: 1 mg sample powders: 0.5 mL of an *E. coli* bacterium combination, were mixed (The colony-counting approach was utilized by the ASTM International E3031-15 guidelines) [55]. The suspension of sample powders and *E. coli* were equally distributed over the LB broth plate by using an L-shaped glass rod. The samples were incubated at 37 °C for 24 h. Following that, a colony counter (Rocker Galaxy 330, Kaohsiung, Taipei, Taiwan) measured the colony's growth and calculated bacterial activity using the following formula:

$$AR = \frac{A - B}{A} \times 100\% \quad (1)$$

The typical number of bacteria per sample before the sample was added is denoted by A, the typical number of bacteria per sample after the sample was added is denoted by B, and the average bacterial rate (%) is denoted by AR.

2.4. In Vitro Bioactivity Test

Samples of the experiment were immersed in simulated body fluid (SBF) to describe the in vitro bioactivity of MBG powder and investigate the effect of pore shape. Kokubo et al. [56] suggested the use of SBF as a solution with a comparable ionic content to human blood plasma. The reagent substances for preparing SBF solution are as follows:

$NaCl$, $NaHCO_3$, KCl, $K_2HPO_4{\cdot}3H_2O$, $MgCl_2{\cdot}6H_2O$, $CaCl_2$, Na_2SO_4, $(CH_2OH)3CNH_2$ and 1M-HCl, each contain 7.996, 0.350, 0.224, 0.228, 0.305, 0.278, 0.071, 6.057 g and 40 mL, respectively. All SBF reagents were mixed into one liter of DI water, and the pH value was adjusted to 7.40 at 37 °C by using a magnetic stirrer. In this study, 1 g of the specimen powders was soaked to 10 mL SBF with the ratio of MBG: SBF = 1:10 for 7 days, and the immersed sample was stored inside a thermostatic shaker at a fixed temperature of 37 °C. Finally, the sample powders were separated in SBF through centrifugation at 5000 rpm for 5 min. Subsequently, the samples underwent two cleaning cycles, each involving 10 mL of double-distilled water and acetone. The SBF was refreshed every 24 h using a centrifuge machine. The samples were dried in an oven at 70 °C for 24 h.

2.5. Cytotoxicity Test

The MTT test steps were performed following the standard procedure of ISO10993-part 5: 2009 [57,58]. The choice to use osteoblast cell lines (MC3T3-E1) is based on their direct relevance to bone tissue and the need to comprehend the influence of bioactive glasses on bone cell activity, thereby imparting significant clinical importance when assessing the cytocompatibility of materials employed in bone surgery [59]. Firstly, the MC3T3-E1 cells (ATCC CRL-2594, Manassas, VA, USA) were cultured in a 75 cm^2 flask using minimum essential medium Alpha (MEM-α, Gibco, Waltham, MA, USA) supplemented with 10% fetal bovine serum (FBS, Gibco, Waltham, MA, USA), 100 g/mL streptomycin, and 100 U/mL penicillin. In this study, 500 µL of MC3T3-E1 osteoblast cells were first planted at a density of 2×10^4 cells per well onto 24-well plates. Next, the cultured cells were incubated at 37 °C for 24 h in a humidified 5% CO_2 atmosphere. Next, 0.5 mg of un-doped, Ag-doped, Ce-doped, and Ag/Ce co-doped MBG powders were immersed into 5 mL of the medium for 72 h at 37 °C with the dilution series of 100 µg mL^{-1}. The media were removed from each well after 72 h of incubation, and 200 µL of MTT solution was added. Each well was then incubated at 37 °C for 4 h to create formazan crystals. The purple crystals were dissolved by adding 300 µL of dimethyl sulfoxide (DMSO, Echo, Taiwan) to each well after the MTT solutions had been withdrawn and the cell viability was determined using a microplate reader (Multiskan Go, Thermo Scientific, Waltham, MA, USA) with a 570 nm absorbance wavelength and then the living and dead cells were calculated to a cell viability of >70% (not toxic). The absorbance value (OD Value) of this standard group was determined as the 100% survival rate of the cell survival rate experiment.

2.6. Statistical Analysis

Each test was performed in triplicate, and the results were presented as mean ± standard deviation. The study has observed statistical significance levels of $n = 3$, * $p < 0.05$ and ** $p < 0.001$ through the utilization of one-way analysis of variance.

3. Results

3.1. Phase Composition

First, the phase compositions of all samples were assessed using X-ray diffraction (XRD), as displayed in Figure 2. The obtained results confirm the amorphous structures of all MBG specimens, except 5.75 mol% Ag-doped MBG. With the higher Ag concentration (the 5.75 mol% Ag case), the XRD pattern exhibited the diffraction peaks at 38.2, 44.4, 64.6, and 77.6°, which correspond to the (111), (200), (220), and (311), respectively, diffraction maximum in silver (Ag, PDF#87-0720), and (116), (314) for silver oxide (Ag_2O), PDF#46–1476). Hence, for the Ag-doped MBG powders, increasing the silver concentration changed from the amorphous structure to crystalline phases, whereas the cerium-doped MBG powders did not.

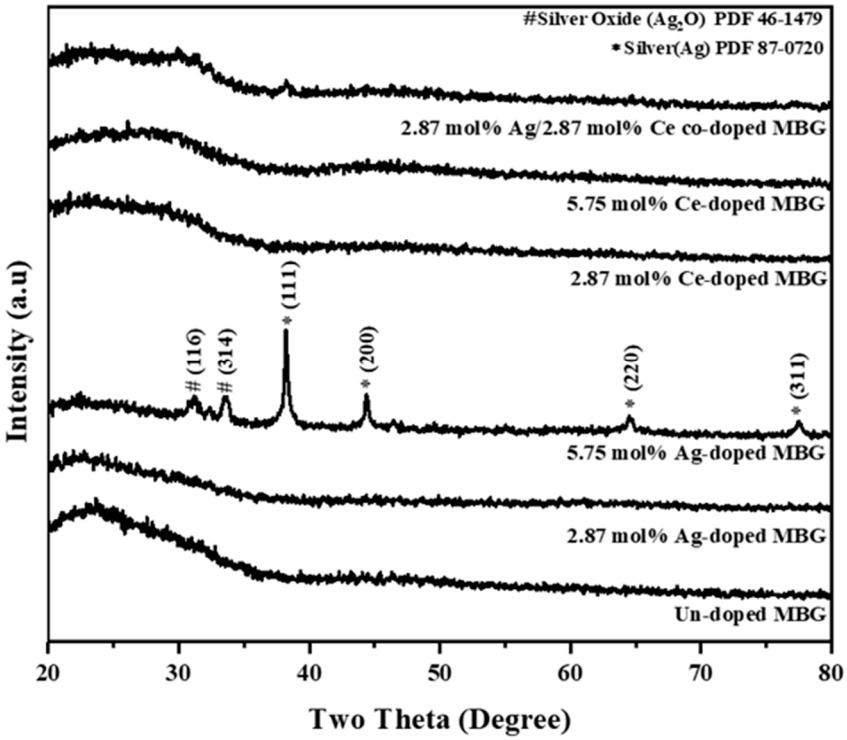

Figure 2. XRD patterns of un-doped MBG, 2.87 mol% Ag-doped, 5.75 mol% Ag-doped, 2.87 mol% Ce-doped, 5.75 mol% Ce-doped, and 2.87 mol% Ag/2.87 mol% Ce co-doped MBG.

3.2. Morphology and Chemical Composition

The SEM images of the doped and co-doped MBG powders are shown in Figure 3. The particle size distributions of un-doped, 2.87Ag-doped, 5.75Ag-doped, 2.87Ce-doped, 5.75Ce-doped, and 2.87Ag/2.87Ce co-doped (mol%) MBG are 671.17 ± 183.46, 602.19 ± 166.28, 663.43 ± 188.44, 646.50 ± 189.83, 668.19 ± 151.87, and 529.81 ± 180.98 nm, respectively, are shown in Figure 4. The elemental composition of materials was determined using EDS, as shown in Table 1. The results demonstrated that all MBG specimens show experimental composition values that are qualitative consistent with the nominal composition values. For doped MBG specimens, the atomic percentage of Ag and Ce is proportional to the dopant concentration. Furthermore, the co-doped MBG specimens showed the presence of both Ag and Ce elements. These results indicated that the dopant of Ag, Ce, and Ag/Ce into the MBG structure was successful.

Table 1. Atomic compositions of un-doped, 2.87 mol% Ag-doped, 5.75 mol% Ag-doped, 2.87 mol% Ce-doped, 5.75 mol% Ce-doped, and 2.87 mol% Ag/2.87 mol% Ce co-doped MBG.

	Atomic Composition (at %)				
Sample Type	**Si**	**Ca**	**P**	**Ag**	**Ce**
Nominal	76.92	15.38	7.69	-	-
Un-doped MBG	71.49 ± 0.69	14.82 ± 0.64	11.63 ± 0.73	2.06 ± 0.52	-
2.87 mol% Ag-doped MBG	69.52 ± 0.33	14.34 ± 0.85	10.07 ± 0.85	6.07 ± 0.69	-
5.75 mol% Ag-doped MBG	71.89 ± 0.41	14.01 ± 0.34	11.07 ± 0.69	-	3.03 ± 0.11
2.87 mol% Ce-doped MBG	68.78 ± 0.28	13.6 ± 0.86	11.79 ± 0.89	-	5.82 ± 0.23
5.75 mol% Ce-doped MBG	69.07 ± 0.37	14.0 ± 0.99	11.01 ± 0.29	2.9 ± 0.35	3.02 ± 0.17
2.87 mol% Ag/2.87 mol% Ce co-doped MBG	71.49 ± 0.69	14.82 ± 0.64	11.63 ± 0.73	2.06 ± 0.52	-

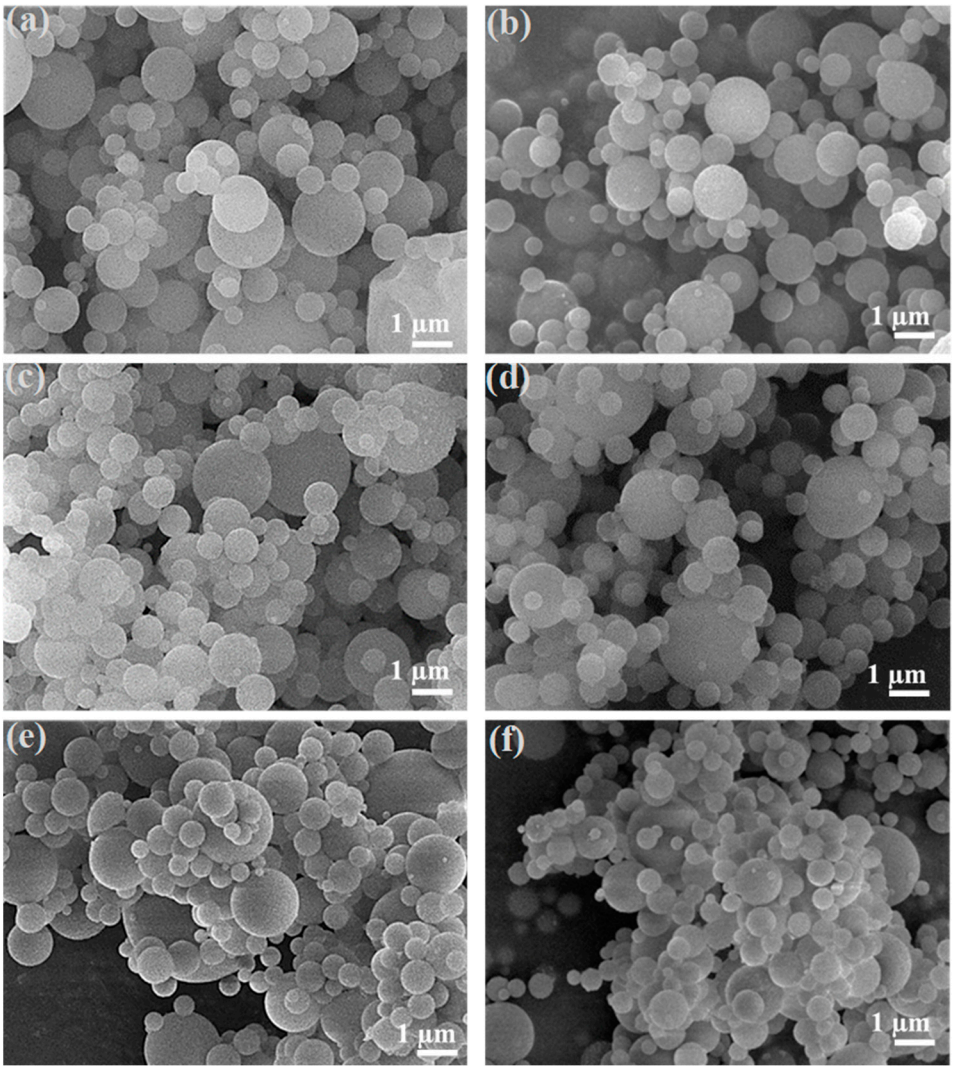

Figure 3. SEM images of (**a**) un-doped MBG, (**b**) 2.87 mol% Ag-doped, (**c**) 5.75 mol% Ag-doped, (**d**) 2.87 mol% Ce-doped, (**e**) 5.75 mol% Ce-doped, and (**f**) 2.87 mol% Ag/2.87 mol% Ce co-doped MBG.

According to our TEM studies (Figure 5), the successful system of spherical mesoporous particles of un-doped MBG is confirmed. Ag-doped, Ce-doped, and Ag-Ce-co-doped MBG all had spherical shapes. In addition, the Ag dopant and Ag nanoparticles were seen on the surface of the particles, as shown in Figure 5b,c. Figure 5f, which also illustrates the result of the Ag/Ce co-doped MBG sample, shows a similar nanostructure to the Ag-doped MBG samples with Ag nanoparticles produced on the particle's surface [52]. Moreover, in Figure 5e, the Ce nanoparticles exhibit that they are noticeably darker than un-doped and Ag-doped MBGs. This observation indicates a higher atomic weight. It is worth noting that Ce possesses an atomic number of 58, while Ag possesses an atomic number of 47. On the other hand, the constituents of un-doped MBG do not possess atomic numbers greater than 20. Furthermore, the MBG samples that were doped with 5.75% Ag, 5.75% Ce, and 2.87% Ag/2.87% Ce (mol%) display darker regions on the MBG particles. These darker regions become more prominent in terms of both quantity and size of nanoparticles as the concentrations of Ag and Ce increase. This suggests a correlation with the growth of metallic Ag and Ce nanoparticles on the glass surface and within the pores.

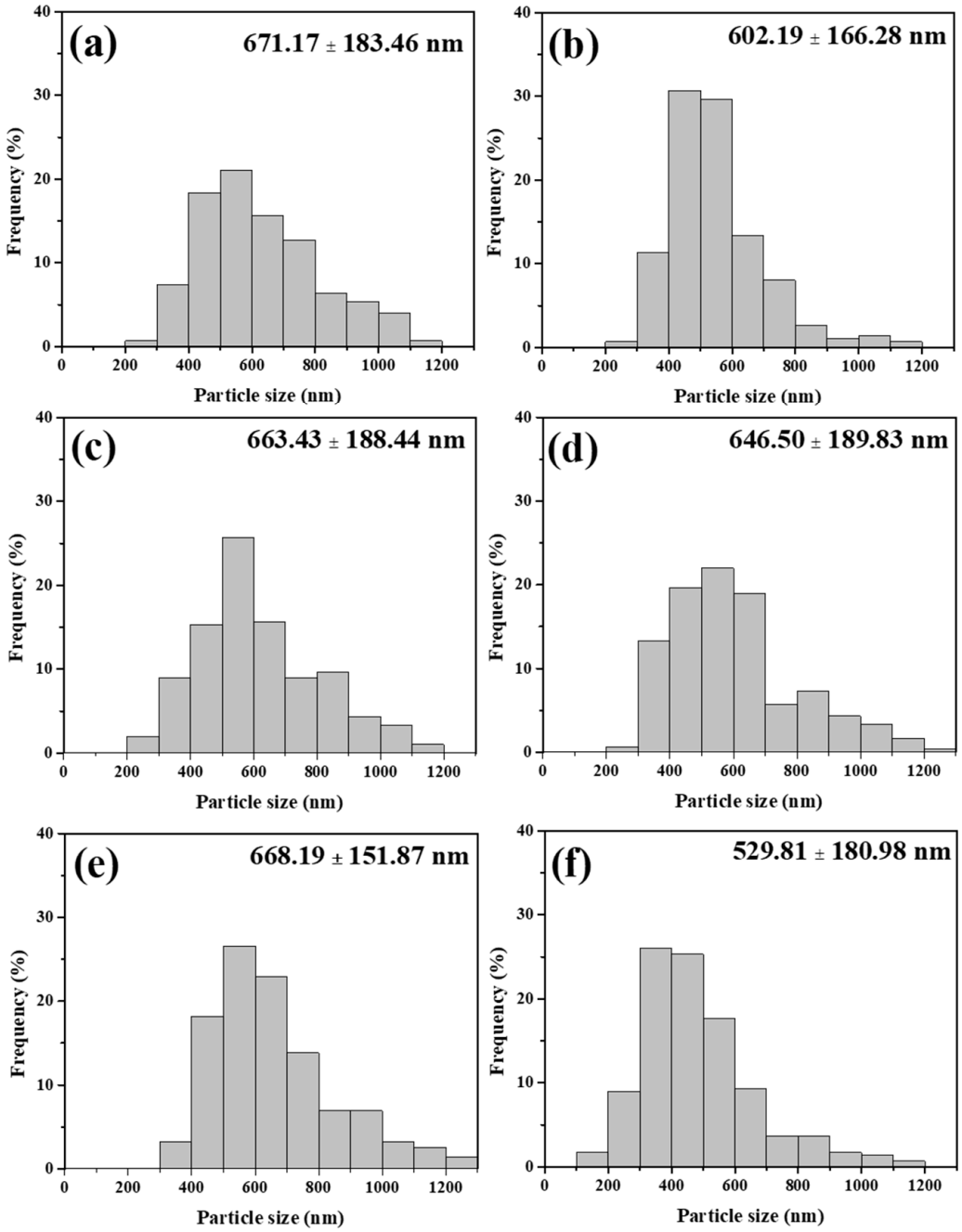

Figure 4. Particle size distributions of (**a**) un-doped MBG, (**b**) 2.87 mol% Ag-doped, (**c**) 5.75 mol% Ag-doped, (**d**) 2.87 mol% Ce-doped, (**e**) 5.75 mol% Ce-doped, and (**f**) 2.87 mol% Ag/2.87 mol% Ce co-doped MBG.

BET and BJH analyzed particular powder specimen sur face areas, typical pore sizes, and pore volumes using physical adsorption and desorption with nitrogen gas, which was utilized because of its availability, inertness, and excellent quality. This research found that all sample powders are mesoporous, with pore diameters averaging 11 nm, and the specific surface area of un-doped, 2.87Ag-doped, 5.75Ag-doped, 2.87Ce-doped, 5.75Ce-doped, and 2.87Ag/2.87Ce co-doped (mol%) MBG was 230.68 ± 10.61, 217.78 ± 13.07, 186.01 ± 7.57, 170.12 ± 19.99, 57.39 ± 1.49, and 191.93 ± 0.54 m^2/g, respectively, as well as the specimen's pore volume (cc/g), which was 0.7227 ± 0.018, 0.6144 ± 0.052, 0.5274 ± 0.026, 0.4822 ± 0.018, 0.2927 ± 0.090, and 0.6225 ± 0.006, as shown Table 2. Moreover, the MBG powders at a higher concentration have a lower specific surface area (for instance,

230.68 m^2/g for the case of an un-doped MBG, but 57.39 m^2/g for the 5.75 mol% Ce-doped MBG case) and pore volume (for instance, 0.7227 cc/g for the case of an un-doped MBG, but 0.2927 cc/g for 5.75 mol% Ce-doped cases). The N_2 sorption isotherms of obtained samples (Figure 6) are type IV characteristic mesoporous materials, and the H1 hysteresis loop indicated the narrow pore-size distribution.

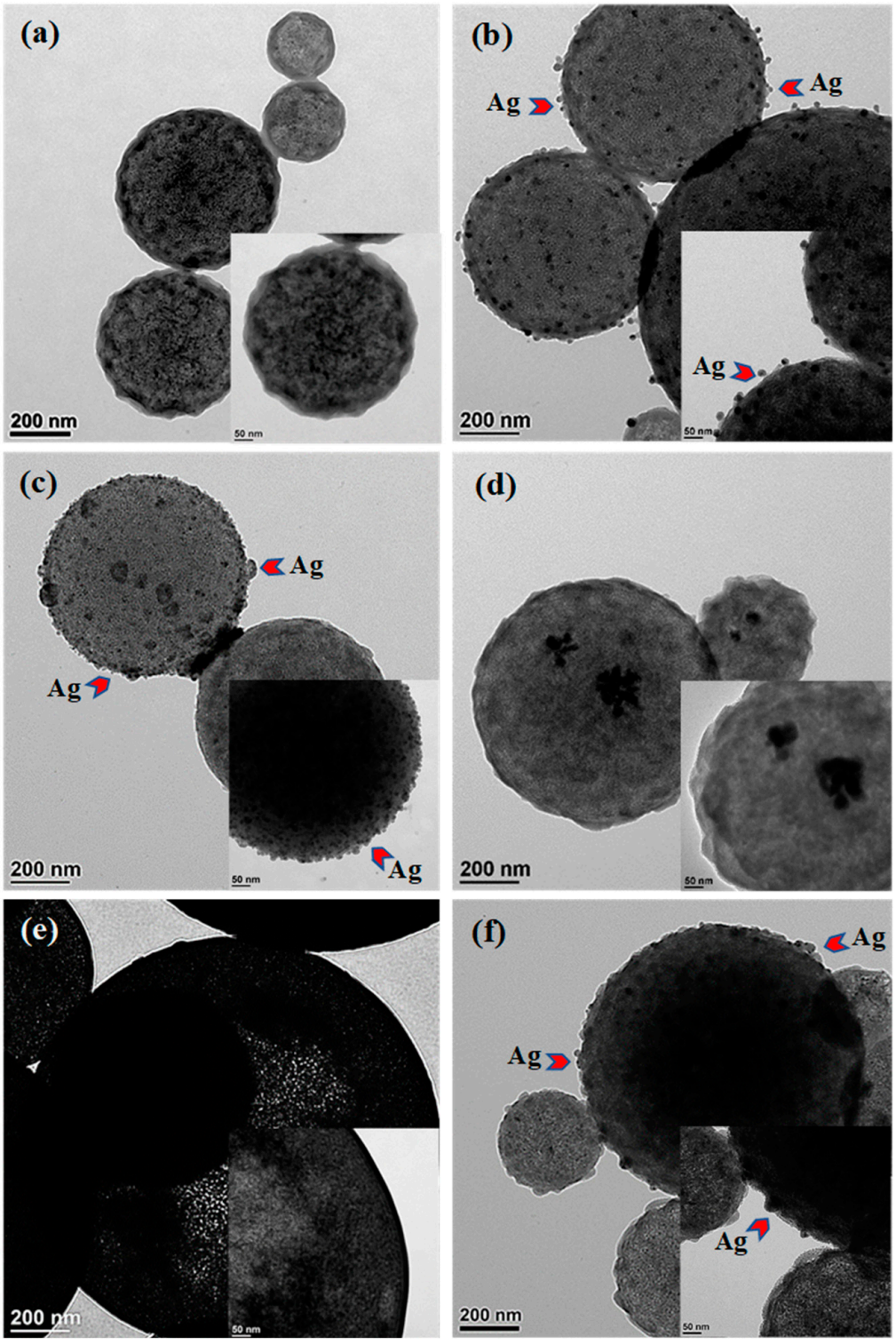

Figure 5. TEM images of (**a**) un-doped MBG, (**b**) 2.87 mol% Ag-doped, (**c**) 5.75 mol% Ag-doped, (**d**) 2.87 mol% Ce-doped, (**e**) 5.75 mol% Ce-doped, and (**f**) 2.87 mol% Ag/2.87 mol% Ce co-doped MBG.

Table 2. Specific surface area, total pore volume, and pore radius of un-doped, 2.87 mol% Ag-doped, 5.75 mol% Ag-doped, 2.87 mol% Ce-doped, 5.75 mol% Ce-doped, and 2.87 mol% Ag/2.87 mol% Ce co-doped MBG.

Sample Type	Specific Surface Area (m^2 g^{-1})	Total Volume (cm^3 g^{-1})	Pore Radius (nm)
Un-doped MBG	230.68 ± 10.61	0.7227 ± 0.018	5.09 ± 2.12
2.87 mol% Ag-doped MBG	217.78 ± 13.07	0.6144 ± 0.052	4.67 ± 1.50
5.75 mol% Ag-doped MBG	186.01 ± 7.57	0.5274 ± 0.026	4.82 ± 1.73
2.87 mol% Ce-doped MBG	170.12 ± 19.99	0.4822 ± 0.018	5.45 ± 1.69
5.75 mol% Ce-doped MBG	57.39 ± 1.49	0.2927 ± 0.090	8.16 ± 0.06
2.87 mol% Ag/2.87 mol% Ce co-doped MBG	191.93 ± 0.54	0.6225 ± 0.006	6.38 ± 0.10

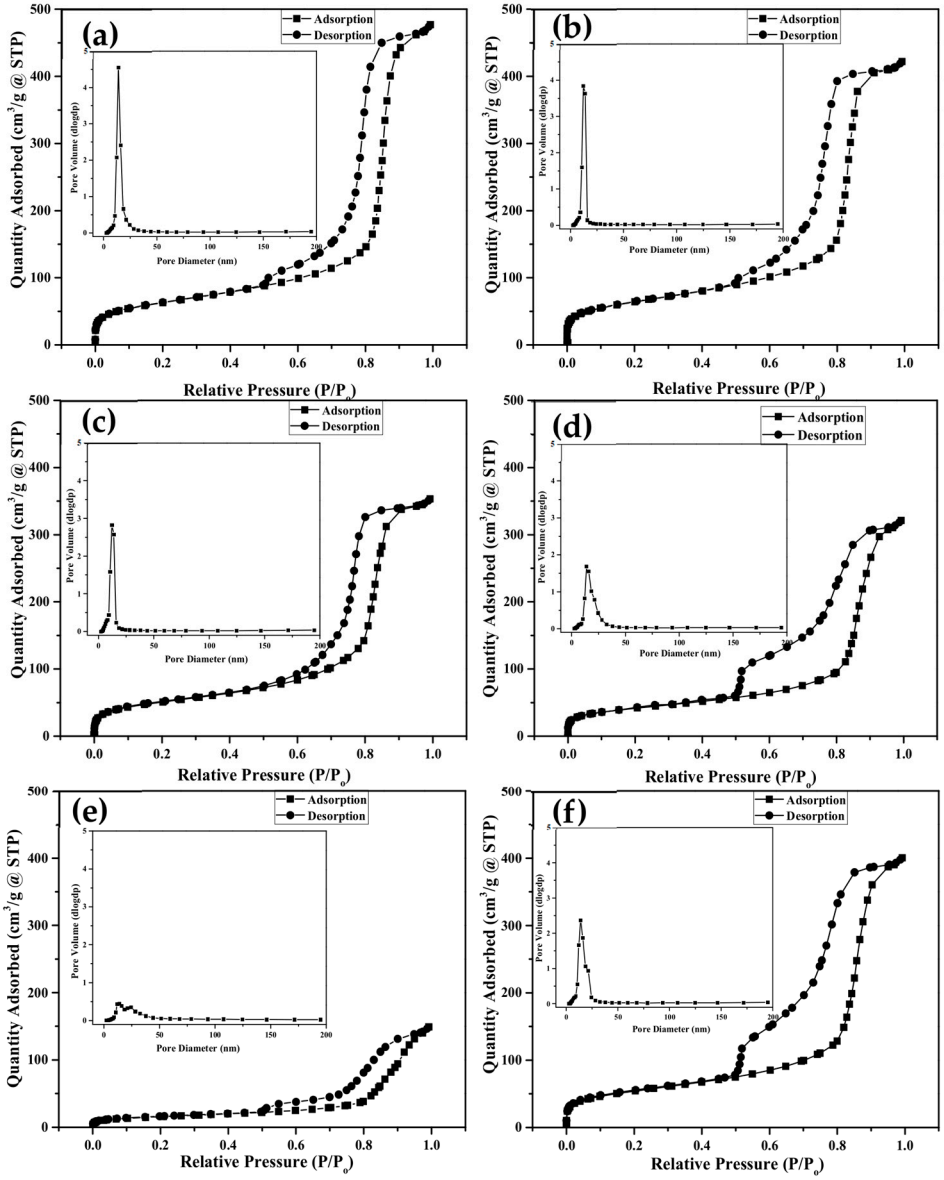

Figure 6. The N2 adsorption–desorption isotherms of (**a**) un-doped MBG, (**b**) 2.87 mol% Ag-doped, (**c**) 5.75 mol% Ag-doped, (**d**) 2.87 mol% Ce-doped, (**e**) 5.75 mol% Ce-doped, and (**f**) 2.87 mol% Ag/2.87 mol% Ce co-doped MBG.

3.3. Antibacterial Activities

Six samples of un-doped, 2.87Ag-doped, 5.75Ag-doped, 2.87Ce-doped, 5.75Ce-doped MBG, and 2.87Ag/2.87Ce co-doped (mol%) MBG bioactive glasses were investigated for antibacterial activity against *E. coli* bacteria. The results showed that 5.75Ag-doped and 2.87Ag/2.87Ce- co-doped (mol%) MBG killed 100% of *E. coli* bacteria after 24 h, whereas 2.87Ag-doped (86.6%) > 5.75Ce-doped (63.33%) > 2.87Ce (6.67%)-doped > un-doped (3%) (mol%) MBG (Figure 7). Thus, the killing efficiency of doped MBGs against *E. coli* bacteria was dependent on their concentrations.

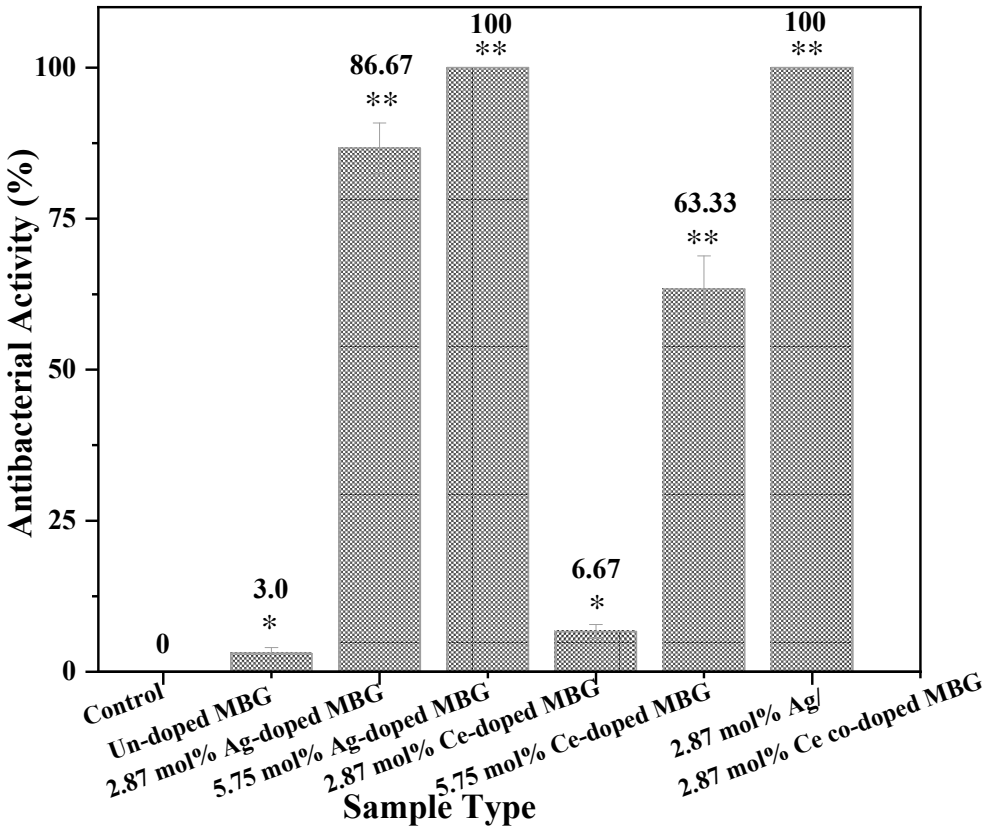

Figure 7. Antibacterial activities of un-doped *MBG*, 2.87 mol% Ag-doped, 5.75 mol% Ag-doped, 2.87 mol% Ce-doped, 5.75 mol% Ce-doped, and 2.87 mol% Ag/2.87 mol% Ce co-doped MBG against *E. coli* bacteria ($n = 3$, * $p < 0.05$ and ** $p < 0.001$).

3.4. In Vitro Bioactivity

XRD, SEM, and FTIR are used to identify calcium phosphate in samples. The amorphous character of the bio-glasses became crystalline as the immersion duration increased up to 7 days, enhancing the crystallinity of HA, silver, and cerium phosphate (monazite). Some new crystalline phases appeared, e.g., HA(PDF#89-6437), silver (PDF#65-2871), and cerium phosphate (PDF#74-1889) were formed after 7 days soaking of SBF in the case of silver and cerium-doping, as shown Figure 8. The SEM images demonstrate that for every MBG following SBF immersion, the surface of all MBG specimens except 5.75 mol% Ce doped MBG, HA crystals were found to develop (Figure 9). In summary, XRD and SEM data verified the development of HA on un-doped, silver-doped, cerium-doped, and silver–cerium co-doped MBG. Furthermore, FTIR analysis was performed to quantify the bioactivity. Figure 10a,b illustrates the FTIR spectra of MBGs before and during their 7-day submersion in SBF solution. According to previous works [60,61], the spectral bands around 482 and 566 cm^{-1} are assigned to HA. To begin with, the spectral band at 482 cm^{-1} is assigned to the Si-O-Si bending vibration (referred to as I_1) [62], while the spectral band at 566 cm^{-1} is assigned to P-O bending vibrations (referred to as I_2) [63]. The intensity

ratio (I_1/I_2) of these peaks was calculated by dividing the intensity of the P-O peak by that Si-O-Si peak. I_1/I_2 ratios of un-doped, 2.87Ag-doped, 5.75Ag-doped, 2.87Ce-doped, 5.75Ce-doped, and 2.87Ag-2.87Ce co-doped (mol%) MBG before immersion of SBF were determined here as 0.114 ± 0.007, 0.151 ± 0.014, 0.186 ± 0.035, 0.148 ± 0.014, 0.103 ± 0.007, and 0.175 ± 0.004 (Figure 10a), whereas the I_1/I_2 ratios after immersion were calculated as 0.214 ± 0.036, 0.252 ± 0.056, 0.283 ± 0.072, 0.236 ± 0.044, 0.209 ± 0.046, and 0.279 ± 0.072, respec tively (Figure 10b).

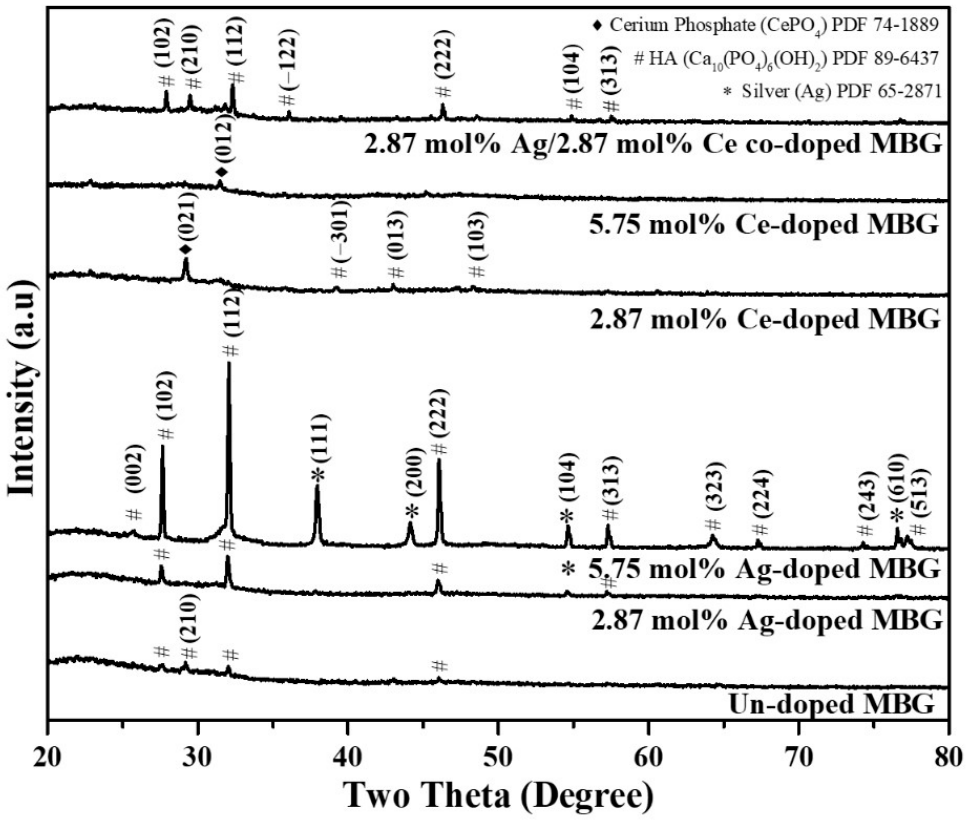

Figure 8. XRD patterns of un-doped MBG, 2.87 mol% Ag-doped, 5.75 mol% Ag-doped, 2.87 mol% Ce-doped, 5.75 mol% Ce-doped, and 2.87 mol% Ag/2.87 mol% Ce co-doped after immersion in the SBF solution for 7 days.

3.5. Cell Viability

At last, the cytotoxicity of MBG samples at concentrations of 100 $\mu g.mL^{-1}$ is assessed and determined using the MTT test after 72 h of contact. According to the standard of ISO10993-5 for cytotoxicity tests, a substance must have a live cell survival rate of >70% to be considered non-toxic. Figure 11: MTT assay test findings for as-received un-doped, 2.87Ag-doped, 5.75Ag-doped, 2.87Ce-doped, 5.75Ce-doped, and 2.87Ag/2.87Ce co-doped (mol%) MBG with cell viability values of 84.83 ± 0.029, 83.53 ± 0.062, 69.28 ± 0.213, 89.51 ± 0.230, 100.01 ± 0.221, and 86.84 ± 0.057%, respectively after 72 h of incubation. As a result, except for 5.75 mol% Ag-doped MBG, all samples are non-toxic on MC3T3-E1 osteoblasts.

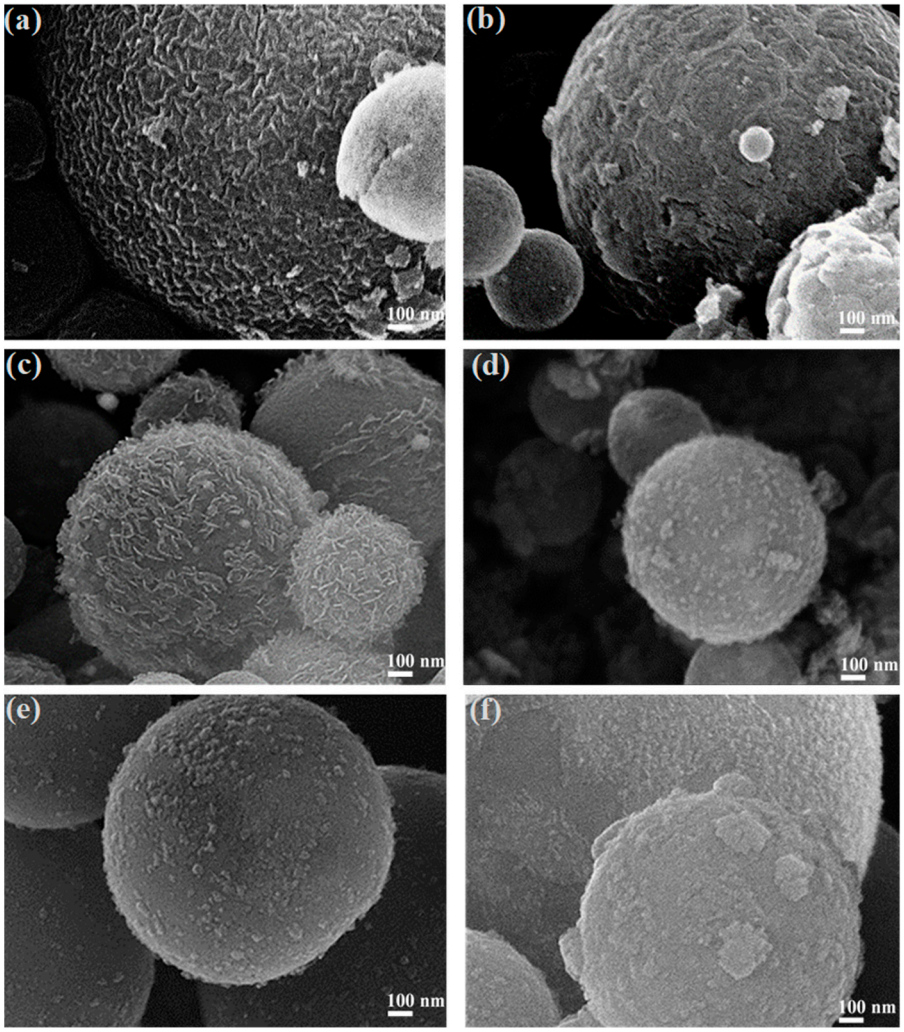

Figure 9. SEM images of (**a**) un-doped MBG, (**b**) 2.87 mol% Ag-doped, (**c**) 5.75 mol% Ag-doped, (**d**) 2.87 mol% Ce-doped, (**e**) 5.75 mol% Ce-doped, and (**f**) 2.87 mol% Ag/2.87 mol% Ce co-doped MBG after immersion in the SBF solution for 7 days showing the HA formation on the surfaces.

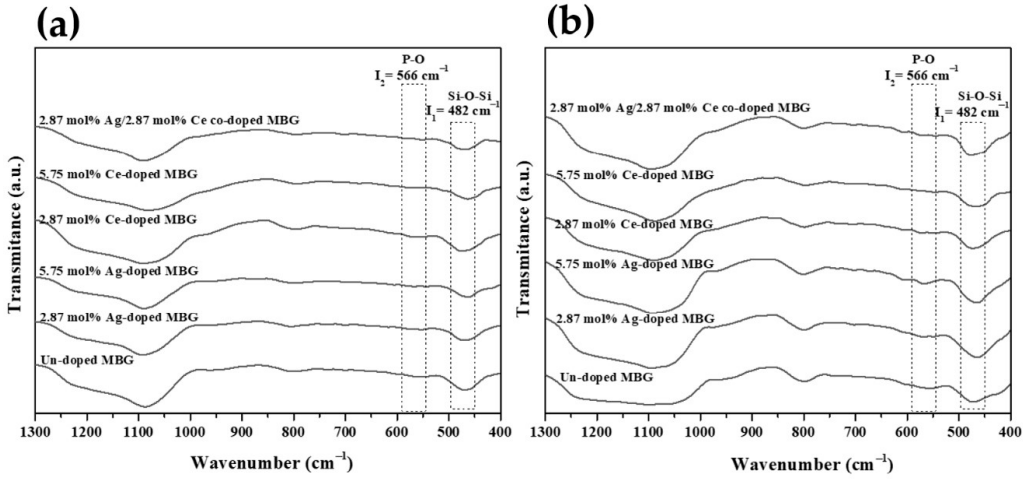

Figure 10. FTIR spectra of un-doped MBG, 2.87 mol% Ag-doped, 5.75 mol% Ag-doped, 2.87 mol% Ce-doped, 5.75 mol% Ce-doped, and 2.87 mol% Ag/2.87 mol% Ce co-doped MBG (**a**) before and (**b**) after immersing in the SBF solution for 7 days.

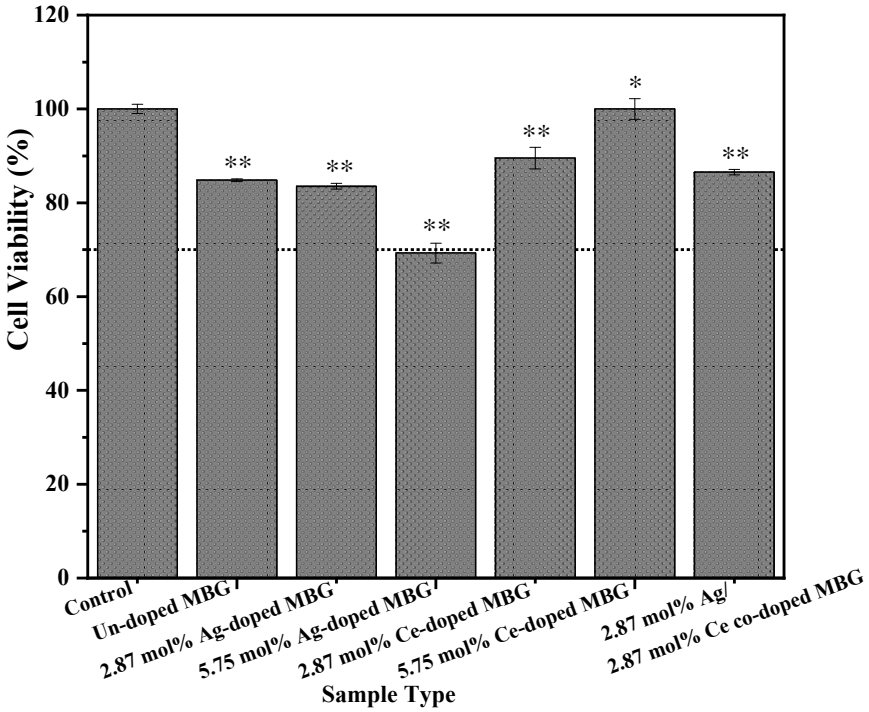

Figure 11. Cell Viability test of un-doped MBG, 2.87 mol% Ag-doped, 5.75 mol% Ag-doped, 2.87 mol% Ce-doped, 5.75 mol% Ce-doped, and 2.87 mol% Ag/2.87 mol% Ce co-doped MBG during 72 h (n = 3, * $p < 0.05$ and ** $p < 0.001$).

4. Discussion

The XRD analysis, Figure 2, revealed that the phase compositions of the MBG specimens treated with varying concentrations (un-doped, Ag-doped, Ce-doped, and Ag-Ce co-doped MBG), HCl acid catalysts, and Pluronic F-127 surfactant were all characterized as amorphous except for the 5.75 mol% Ag-doped MBG. These findings suggest that the MBG specimens were successfully synthesized and that the concentration treatments had no effect on the chemical or phase composition of the spray-pyrolyzed MBG specimens, except for 5.75 mol% Ag-doped MBG. Furthermore, according to the FE-SEM morphology figures (Figure 3), all MBG specimens have a smoothed sphere morphology with no irregular shapes and nanosized particles (less than 100 nm) formed, indicating that un-doped, Ag-doped, Ce-doped, and Ag-Ce co-doped MBG specimens went through the "gas-to-particle" conversion rather than the "one-particle-per-droplet" conversion [64].

Table 2 shows the surface area, pore volume, and pore size statistics. At high relative pressures, all MBG samples display type IV isotherms, indicative of a mesoporous structure, with type H1 hysteresis loops and a strong capillary condensation step, as shown in Figure 6. As a result of the produced Si-O-Ag or Ce bonds taking up more space in the mesoporous channels, the pore volume and specific surface area decreased (the addition of silver and cerium disrupted the structure of the mesoporous silica) [65] when we increased the concentration of Ag and Ce ions. However, the mesoporous materials' distinctive textural features imply that the surface properties, particularly the ultrahigh specific surface area, play a significant role in enhancing the apatite-forming ability [2]. The formation of apatite is significantly accelerated by ultrahigh-specific surface area (over 100 m^2/g [66]), and this material has unique features that make it particularly appealing for biomedical applications. As a result, all MBGs exhibited remarkably high specific surface areas, with the exception of the 5.75 mol% Ce-doped MBG, which demonstrated a considerably lower specific surface area, approximately one-third of the other samples. The remaining MBGs were specifically developed for applications involving bone defects. Besides the specific surface area, the concentration of the dopant played an essential role in influencing the surface characteristics

and the surface chemistry, which, consequently, exerted a substantial influence on bacterial activity and in vitro bioactivity.

Significantly, the results of our study emphasize the antibacterial effectiveness of dopants, which is dependent on their concentration. The un-doped MBG demonstrated the least effectiveness, with a reduction of only 3%. This emphasizes the importance of doping in enhancing the potential for antibacterial activity. Moving up the scale, the MBG doped with 2.87 mol% of cerium displayed limited bactericidal activity at 6.67%, suggesting that cerium ions alone may not be as effective against *E. coli*. In contrast, the MBG doped with 5.75 mol% of cerium exhibited moderate antibacterial effects with a reduction of 63.33%, indicating the potential of cerium ions. Additionally, the MBG doped with 2.87 mol% of silver demonstrated significant efficacy, eliminating 86.6% of *E. coli*, thereby emphasizing the role of silver ions. The most impressive bactericidal performance was observed in the MBG doped with 5.75 mol% of silver and the MBG co-doped with 2.87 mol% of silver and 2.87 mol% of cerium, as they completely eradicated *E. coli* within 24 h. This can be attributed to the strong antibacterial properties of silver ions. Importantly, the results of our study emphasize the effectiveness of dopants in preventing bacterial growth, which is dependent on their concentration. Additionally, our investigation has taken into account the findings of previous studies. In the prior research on antibacterial properties, it was established that cerium-containing compounds exhibit antibacterial effects by inhibiting both glucose oxidation and absorption, along with the modulation of endogenous respiration [33]. According to recent research, the glass composition, local pH, dose, duration of treatment, shape, surface chemistry, particle size, and presence of surface coatings are some of the parameters that affect cerium's antibacterial properties [67,68]. A stronger antibacterial property was detected when the quantity of cerium oxide was in the 5 to 10 mol% range at the concentration of 10 mg/mL and above [69]. Youness et al. [70] discovered that increasing the cerium concentration of phosphate glasses improved their antibacterial effectiveness against *E. coli*. Raimondi et al. investigated the antibacterial properties of cerium-doped MBGs up to 5.3 mol% concentration [33]. Despite the conclusion made by Garner et al. [71], that cerium has weak antibacterial activities at low concentrations of cerium [72]. According to Chen et al., the cerium (III) ion [73] attaches to *E. coli* cells, blocks endogenous respiration, enters the cells' cytoplasm, and disrupts their metabolic processes [74]. It should be highlighted that the presence of Ce^{3+} and Ce^{4+} may be responsible for the improved antibacterial activities observed. The conversion of cerium (IV) to cerium (III) that occurs after ceria particle adsorption at the surface of *E. coli* cells suggests that oxidative stress may be a plausible mechanism by which cerium particle exerts their toxicity [75]. Because it may act through two different mechanisms: ionic and particle effects, the Ce-doped MBG produced in this work is thought to have antibacterial characteristics during 24 h at 2 mg/mL concentration, as shown in Figure 6. The ionic effect may aid in maintaining the material's antibacterial properties if one of the pathways was hindered by an environmental factor, such as when particle impacts were reduced after interacting with or aggregating with other particles in the medium [76]. The enhanced antibacterial effectiveness of Ag-MBG in comparison to Ce-doped MBG can be attributed to the enhancement of silver's antibacterial characteristics via thiol groups [77]. The thiol groups of cysteine residues, which are crucial for the operation of many enzymes, are subjected to numerous conformational changes as a result of this linkage, which ultimately renders bacterial enzymatic activity inactive. For instance, DNA replication is hampered by the increased pyrimidine dimerization caused by the attaching of Ag^{+} to the guanine base (N7 atom) [78,79] and the antibacterial properties of silver nanoparticles are influenced by factors including their morphology (as shown in TEM images) and nanoparticle size. Further, the reaction mechanisms underlying the action of silver and cerium ion-doped or co-doped MBG within the bacterial membrane. Our investigation revealed that these doped MBGs induce the generation of reactive oxygen species (ROS) within *E. coli* bacterial cells. This production of ROS occurs as a result of the presence of silver and cerium ions, as well as silver and cerium nanoparticles. The

resultant oxidative stress serves as a pivotal mechanism for the effective eradication of *E. coli* bacteria. The intricate interplay between these elements contributes to the potent antimicrobial action of silver and cerium-doped MBGs, ultimately leading to the successful elimination of *E. coli* bacteria [80,81].

For the bioactivity part of the in vitro study, the bioactivity of the 5.75 mol% Ce-doped MBG sample was slower than that of the un-doped, Ag-doped, 2.87 mol% Ce-doped, and Ag/Ce co-doped MBG sample, but the addition of 5.75 mol% Ce-doped MBG did not significantly modify the capacity of crystallinity production [82]. According to a thorough investigation by Lusvardi et al. [83] on the effect of cerium on bioactivity, cerium addition slows down the development of the HA layer primarily because it produces insoluble crystalline $CePO_4$ and increases chemical durability. Additionally, this impact is connected with the sample's ceria content (concentration): at a ceria level of up to 5.3 mol%, HA production was delayed by up to 28 days, but at a ceria content of up to 1 mol%, HA formation was apparent after 7–14 days [33,84]. Hence, the bioactivity of cerium-doped MBG at higher concentrations requires additional days to develop HA whereas the HA formation of Ag-doped MBG was highest. Shih et al. [53] conducted research by using the XRD peak intensities of the highest peak that has the highest HA (2 θ = 32.07 and 29.23°); we compared the XRD peak intensity of the results and found that the bioactivities of the specimens could be categorized as un-doped, Ag-doped, Ce-doped, and Ag-Ce co-doped MBG from 5.75Ag-doped > 2.87Ag/2.87Ce co-doped > 2.87Ag-doped > 2.87Ce-doped > un-doped > 5.75Ce-doped (mol%) MBG. This result demonstrates that Ag dopants will increase Ag-doped MBG's bioactivity, speeding up HA growth rates (Figure 8). The other confirmation study of bioactivity was FTIR and SEM morphology. Figure 10 shows the FTIR spectra of un-doped, doped, and co-doped MBGs. The expansion of infrared absorption bands of Si-O-Si stretching vibration is increasingly evident with an increase in the silver content and low content of Ce-doped MBG in glass systems. Ag- and Ce-doped MBGs have XRD patterns that show the presence of hydroxyapatite, metallic silver, and cerium phosphate, which suggests that these materials disrupt the connection of the Si-O-Si glass network. As a result, the FTIR results validated that all MBGs were bioactive in vitro, except 5.75 mol% Ce-doped MBG after 7 days of soaking in SBF, supporting the XRD and SEM (observed the HA morphology, see Figure 9) findings. We will now look at why Ag increases MBG bioactivity. One of the crucial factors in developing novel glass composition designs is, therefore, taking the chemical structure of the glass into account, as doing so would alter the glass's bioactivity. The SiO_4 tetrahedral network forms the basis of the SiO_2-CaO-P_2O_5 composition, and the O ions link the individual tetrahedral units to create a three-dimensional structure. The degree of connection in the 3D structure is known to be modified by Ca to create non-bridging oxygen (NBO) groups. These NBO groups are necessary for the exchange with H^+ or H_3O from the surrounding SBF solution to generate a high dissolution rate, which leads to a high HA production (the first stage in the process of HA creation is the dissolution of bioglass surface) [85]. Vernè et al. [86] and Lin et al. [87] conducted investigations where they first synthesized BG and then coated Ag at the BG surface to create Ag-containing MBG. The majority of Ag is present at the BG surface and does not interact with the BG structure to reduce the quantity of NBO groups [88]. The Ag ions produced from the Ag particles at the BG surface act as the nucleus of HA [87], which subsequently accelerates the HA production to offer greater bioactivity when the Ag-containing MBG (Figure 5b,c,f) is submerged in SBF. The majority of the Ag particles were present at the surface of the Ag-containing MBG powders used in this investigation, in which the dissolution rate of the Ag solubility rate is higher thus accelerating the ion exchange and speeding up the HA formation. For the other study, El-Kady et al. [89] employed sol-gel to make the Ag-containing BG particles, and most of the Ag ions were integrated into the glass structure, which allowed them to study the retardation of bioactivity. The Ag-O bonds are therefore anticipated to be more covalent than the Ca-O ones [89]. Hence, silver (monovalent) would thus be used in place of calcium (bivalent) to reduce the dissolving of the glass because silver ions had greater

electronegativity than calcium ions. Silica ions release rates were assessed as a sign of glass dissolving to further support the idea that the addition of silver has reduced glass dissolution. The results showed that as the silver concentration in the glasses grew, silica release rates from their surfaces dropped [89]. For this situation, Ag may reduce the quantity and nature of the glass groups [88], which would slow down the synthesis of HA and result in a reduction in bioactivity. This was likewise the case with cerium ions, as shown Figure 5d,e, where most Ce particles were not visible on the BG surface.

The MTT assay test was the final investigation for this study. Silver may be dangerous if discharged in large amounts, thus it is important to carefully monitor how much is injected. The potential of ion-exchange treatments to surface functionalize glasses while maintaining the bulk structure and primary characteristics of MBG is well recognized [34]. According to a study by Chao Shi et al., when the Ag-doping concentration increases from 0.04 to 197 μg mL^{-1}, the antibacterial rate improves from 63% to 99% but cell viability reduces from 97% to 62% [90]. Furthermore, Luo et al. also developed in vitro testing on osteoblasts and fibroblasts, and their study revealed no harmful effects from the inclusion of 0.75 and 1 wt% Ag_2O; however, 2 wt% Ag_2O was toxic [91]. When we investigated, all materials were not toxic at a concentration of 100 μg mL^{-1}, but 5.75 mol% Ag-doped MBG was toxic to MT3C3-E1 osteoblast cells after 72 h; therefore, we had to utilize co-doped Ag-Ce MBG, which led to 100% death for *E. coli* bacteria and had no toxic effects on MT3C3-E1 osteoblasts cells, as shown Figure 11.

As the result of this study, co-doped MBGs could offer superior benefits, such as enhanced bioactivity and antibacterial activity. This makes them more effective compared to doped or un-doped MBGs. Hence, co-doped Ag and Ce MBG should be utilized to decrease the issue of Ag toxicity in MBGs and enhance Ce's bacterial killing effectiveness and bioactivity, that is why we examined Ag-Ce co-doped MBG.

In our contemplation of the forthcoming period, the subsequent stages of investigation will encompass the exploration of their associations with varied cell classifications, the elucidation of their operational processes in opposition to additional drug-resistant bacteria, the enhancement of doping concentrations for refined biocompatibility, and the evaluation of their performance within a living organism (in vivo performance), thus establishing the foundation for their potential clinical applications.

5. Conclusions

The objective of this investigation was to enhance the functionality of mesoporous bioactive glasses (MBGs) by incorporating metallic ions, specifically silver (Ag), cerium (Ce), and a combination of Ag and Ce, using the spray pyrolysis technique. This study sought to assess the efficacy of modified MBG particles in addressing bone deformities and bacterial infections in bone repair procedures. It was observed that both 5.75 mol% Ag-doped MBGs and Ag-Ce co-doped MBGs exhibited potent antibacterial properties, effectively eliminating 100% of *E. coli* bacteria after a 24 h incubation period. This finding is particularly significant in the context of bone surgeries, where infections pose critical concerns. Although the antibacterial activity of Ce-doped MBGs was comparatively lower than that of Ag-doped MBGs, further investigation is warranted. The selection of Ag and Ce as metallic ions was based on their known osteogenic properties, which contribute to the enhanced bioactivity of MBGs. Furthermore, the MBGs demonstrated mesoporosity and high reactivity in simulated body fluid (SBF), promoting the formation of a hydroxyapatite layer that resembles bone. In terms of biocompatibility, all MBG compositions, with the exception of the 5.75 mol% Ag-doped MBG, exhibited high compatibility with MC3T3-E1 osteoblasts at a concentration of 100 μg/mL.

Author Contributions: Conceptualization, S.-J.S.; methodology, M.B.T.; validation, S.-J.S. and H.S.N.; formal analysis, M.B.T. and H.S.N.; investigation, M.B.T.; data curation, M.B.T.; writing—original draft preparation, S.-J.S., M.B.T. and H.S.N.; writing—review and editing, S.-J.S. and H.S.N.; supervision, S.-J.S.; project administration and funding acquisition, S.-J.S. All authors have read and agreed to the published version of the manuscript.

Funding: This work was funded by the National Science and Technology Council of Taiwan (grants numbers of NSTC 111-2221-E-011-117- and 112-2221-E-011-040-).

Institutional Review Board Statement: Not applicable.

Informed Consent Statement: Not applicable.

Data Availability Statement: All datasets are publicly available.

Conflicts of Interest: The authors declare that they have no conflict of interest.

References

1. Kargozar, S.; Montazerian, M.; Hamzehlou, S.; Kim, H.-W.; Baino, F. Mesoporous bioactive glasses: Promising platforms for antibacterial strategies. *Acta Biomater.* **2018**, *81*, 1–19. [CrossRef]
2. Migneco, C.; Fiume, E.; Verné, E.; Baino, F. A guided walk through the world of mesoporous bioactive glasses (MBGs): Fundamentals, processing, and applications. *Nanomaterials* **2020**, *10*, 2571. [CrossRef] [PubMed]
3. Hoppe, A.; Güldal, N.S.; Boccaccini, A.R. A review of the biological response to ionic dissolution products from bioactive glasses and glass-ceramics. *Biomaterials* **2011**, *32*, 2757–2774. [CrossRef] [PubMed]
4. Huang, Y.-C.; Lin, T.-Y.; Huang, S.-C.; Yang, T.-Y.; Shih, C.-J. Copper-enhanced silver releasing from bimetal-containing bioactive glass (AgCu/80S) elicits antibacterial efficacy against drug-resistant Staphylococcus aureus. *J. Non-Cryst. Solids* **2022**, *584*, 121509. [CrossRef]
5. Sondi, I.; Salopek-Sondi, B. Silver nanoparticles as antimicrobial agent: A case study on *E. coli* as a model for Gram-negative bacteria. *J. Colloid Interface Sci.* **2004**, *275*, 177–182. [CrossRef] [PubMed]
6. Yoon, K.-Y.; Byeon, J.H.; Park, J.-H.; Hwang, J. Susceptibility constants of *Escherichia coli* and *Bacillus subtilis* to silver and copper nanoparticles. *Sci. Total Environ.* **2007**, *373*, 572–575. [CrossRef]
7. Zhao, G.; Stevens, S.E. Multiple parameters for the comprehensive evaluation of the susceptibility of *Escherichia coli* to the silver ion. *Biometals* **1998**, *11*, 27–32. [CrossRef]
8. Matsumoto, N.; Sato, K.; Yoshida, K.; Hashimoto, K.; Toda, Y. Preparation and characterization of β-tricalcium phosphate co-doped with monovalent and divalent antibacterial metal ions. *Acta Biomater.* **2009**, *5*, 3157–3164. [CrossRef]
9. O'neill, J. Antimicrobial Resistance: Tackling a Crisis for the Health and Wealth of Nations. The Review on Antimicrobial Resistance Chaired by Jim O'Neill. Available online: https://wellcomecollection.org/works/rdpck35v (accessed on 4 October 2023).
10. Bhattacharjee, B.; Ghosh, S.; Patra, D.; Haldar, J. Advancements in release-active antimicrobial biomaterials: A journey from release to relief. *Wiley Interdiscip. Rev. Nanomed. Nanobiotechnol.* **2022**, *14*, e1745. [CrossRef]
11. O'Neill, J. *Tackling Drug-Resistant Infections Globally: Final Report and Recommendations*; Government of the United Kingdom: London, UK, 2016.
12. Tacconelli, E.; Carrara, E.; Savoldi, A.; Harbarth, S.; Mendelson, M.; Monnet, D.L.; Pulcini, C.; Kahlmeter, G.; Kluytmans, J.; Carmeli, Y. Discovery, research, and development of new antibiotics: The WHO priority list of antibiotic-resistant bacteria and tuberculosis. *Lancet Infect. Dis.* **2018**, *18*, 318–327. [CrossRef]
13. Ventola, C.L. The antibiotic resistance crisis: Part 1: Causes and threats. *Pharm. Ther.* **2015**, *40*, 277–283.
14. Awasthi, R.; Rakholia, V.; Agrawal, S.; Dhingra, L.S.; Nagori, A.; Kaur, H.; Sethi, T. Estimating the impact of health systems factors on antimicrobial resistance in priority pathogens. *J. Glob. Antimicrob. Resist.* **2022**, *30*, 133–142. [CrossRef] [PubMed]
15. Predoi, D.; Iconaru, S.L.; Predoi, M.V.; Groza, A.; Gaiaschi, S.; Rokosz, K.; Raaen, S.; Negrila, C.C.; Prodan, A.-M.; Costescu, A. Development of cerium-doped hydroxyapatite coatings with antimicrobial properties for biomedical applications. *Coatings* **2020**, *10*, 516. [CrossRef]
16. Foster, T.J. Antibiotic resistance in Staphylococcus aureus. Current status and future prospects. *FEMS Microbiol. Rev.* **2017**, *41*, 430–449. [CrossRef]
17. Al-Ishaq, R.K.; Skariah, S.; Büsselberg, D. Bacteriophage treatment: Critical evaluation of its application on World Health Organization priority pathogens. *Viruses* **2020**, *13*, 51. [CrossRef]
18. Morris, S.; Cerceo, E. Trends, epidemiology, and management of multi-drug resistant gram-negative bacterial infections in the hospitalized setting. *Antibiotics* **2020**, *9*, 196. [CrossRef]
19. Hrynyshyn, A.; Simões, M.; Borges, A. Biofilms in surgical site infections: Recent advances and novel prevention and eradication strategies. *Antibiotics* **2022**, *11*, 69. [CrossRef]
20. Aslam, B.; Khurshid, M.; Arshad, M.I.; Muzammil, S.; Rasool, M.; Yasmeen, N.; Shah, T.; Chaudhry, T.H.; Rasool, M.H.; Shahid, A. Antibiotic resistance: One health one world outlook. *Front. Cell. Infect. Microbiol.* **2021**, *11*, 771510. [CrossRef]
21. Taye, M.B. Biomedical applications of ion-doped bioactive glass: A review. *Appl. Nanosci.* **2022**, *12*, 3797–3812. [CrossRef]
22. Jung, W.K.; Koo, H.C.; Kim, K.W.; Shin, S.; Kim, S.H.; Park, Y.H. Antibacterial activity and mechanism of action of the silver ion in Staphylococcus aureus and *Escherichia coli*. *Appl. Environ. Microbiol.* **2008**, *74*, 2171–2178. [CrossRef]
23. Mijnendonckx, K.; Leys, N.; Mahillon, J.; Silver, S.; Van Houdt, R. Antimicrobial silver: Uses, toxicity and potential for resistance. *Biometals* **2013**, *26*, 609–621. [CrossRef]

24. Klueh, U.; Wagner, V.; Kelly, S.; Johnson, A.; Bryers, J. Efficacy of silver-coated fabric to prevent bacterial colonization and subsequent device-based biofilm formation. *J. Biomed. Mater. Res. Off. J. Soc. Biomater. Jpn. Soc. Biomater. Aust. Soc. Biomater. Korean Soc. Biomater.* **2000**, *53*, 621–631. [CrossRef]
25. Rai, M.K.; Deshmukh, S.; Ingle, A.; Gade, A. Silver nanoparticles: The powerful nanoweapon against multidrug-resistant bacteria. *J. Appl. Microbiol.* **2012**, *112*, 841–852. [CrossRef] [PubMed]
26. Sales, D.A.; Marques, T.M.; Ghosh, A.; Gusmão, S.B.; Vasconcelos, T.L.; Luz-Lima, C.; Ferreira, O.P.; Hollanda, L.M.; Lima, I.S.; Silva-Filho, E.C. Synthesis of silver-cerium titanate nanotubes and their surface properties and antibacterial applications. *Mater. Sci. Eng. C* **2020**, *115*, 111051. [CrossRef] [PubMed]
27. Anastasiou, A.; Nerantzaki, M.; Gounari, E.; Duggal, M.; Giannoudis, P.; Jha, A.; Bikiaris, D. Antibacterial properties and regenerative potential of Sr^{2+} and Ce^{3+} doped fluorapatites; a potential solution for peri-implantitis. *Sci. Rep.* **2019**, *9*, 14469. [CrossRef]
28. Farag, M.M.; Al-Rashidy, Z.M.; Ahmed, M.M. In vitro drug release behavior of Ce-doped nano-bioactive glass carriers under oxidative stress. *J. Mater. Sci. Mater. Med.* **2019**, *30*, 18. [CrossRef]
29. Liu, J.; Zhou, X.; Zhang, Y.; Zhu, W.; Wang, A.; Xu, M.; Zhuang, S. Rapid hemostasis and excellent antibacterial cerium-containing mesoporous bioactive glass/chitosan composite sponge for hemostatic material. *Mater. Today Chem.* **2022**, *23*, 100735. [CrossRef]
30. Zhu, H.; Zheng, K.; Boccaccini, A.R. Multi-functional silica-based mesoporous materials for simultaneous delivery of biologically active ions and therapeutic biomolecules. *Acta Biomater.* **2021**, *129*, 1–17. [CrossRef]
31. Pei, P.; Qi, X.; Du, X.; Zhu, M.; Zhao, S.; Zhu, Y. Three-dimensional printing of tricalcium silicate/mesoporous bioactive glass cement scaffolds for bone regeneration. *J. Mater. Chem. B* **2016**, *4*, 7452–7463. [CrossRef]
32. Shen, Q.; Qi, Y.; Kong, Y.; Bao, H.; Wang, Y.; Dong, A.; Wu, H.; Xu, Y. Advances in copper-based biomaterials with antibacterial and osteogenic properties for bone tissue engineering. *Front. Bioeng. Biotechnol.* **2022**, *9*, 795425. [CrossRef]
33. Atkinson, I.; Seciu-Grama, A.M.; Petrescu, S.; Culita, D.; Mocioiu, O.C.; Voicescu, M.; Mitran, R.-A.; Lincu, D.; Prelipcean, A.-M.; Craciunescu, O. Cerium-containing mesoporous bioactive glasses (MBGs)-derived scaffolds with drug delivery capability for potential tissue engineering applications. *Pharmaceutics* **2022**, *14*, 1169. [CrossRef] [PubMed]
34. Kaya, S.; Cresswell, M.; Boccaccini, A.R. Mesoporous silica-based bioactive glasses for antibiotic-free antibacterial applications. *Mater. Sci. Eng. C* **2018**, *83*, 99–107. [CrossRef] [PubMed]
35. Wu, C.; Chang, J. Multifunctional mesoporous bioactive glasses for effective delivery of therapeutic ions and drug/growth factors. *J. Control. Release* **2014**, *193*, 282–295. [CrossRef] [PubMed]
36. Wu, C.; Chang, J. A review of bioactive silicate ceramics. *Biomed. Mater.* **2013**, *8*, 032001. [CrossRef] [PubMed]
37. Fada, R.; Farhadi Babadi, N.; Azimi, R.; Karimian, M.; Shahgholi, M. Mechanical properties improvement and bone regeneration of calcium phosphate bone cement, Polymethyl methacrylate and glass ionomer. *J. Nanoanal.* **2021**, *8*, 60–79.
38. Li, H.; Xia, P.; Pan, S.; Qi, Z.; Fu, C.; Yu, Z.; Kong, W.; Chang, Y.; Wang, K.; Wu, D.; et al. The advances of ceria nanoparticles for biomedical applications in orthopaedics. *Int. J. Nanomed.* **2020**, *15*, 7199–7214. [CrossRef] [PubMed]
39. Vallet-Regí, M.; Garcia, M.M.; Colilla, M. *Biomedical Applications of Mesoporous Ceramics: Drug Delivery, Smart Materials and Bone Tissue Engineering*; CRC Press: Boca Raton, FL, USA, 2012.
40. Vallet-Regí, M.; Navarrete, D.A. *Nanoceramics in Clinical Use: From Materials to Applications*; Royal Society of Chemistry: London, UK, 2015.
41. Fan, F.-Y.; Chen, M.-S.; Wang, C.-W.; Shih, S.-J.; Chen, C.-Y.; Pan, Y.-N.; Lin, C.-K. Preparation and characterization of silver nanocrystals decorated mesoporous bioactive glass via synchrotron X-ray reduction. *J. Non-Cryst. Solids* **2016**, *450*, 128–134. [CrossRef]
42. Li, R.; Clark, A.E.; Hench, L.L. An investigation of bioactive glass powders by sol-gel processing. *J. Appl. Biomater.* **1991**, *2*, 231–239. [CrossRef]
43. Tranquillo, E.; Bollino, F. Surface modifications for implants lifetime extension: An overview of sol-gel coatings. *Coatings* **2020**, *10*, 589. [CrossRef]
44. Ardekani, S.R.; Aghdam, A.S.R.; Nazari, M.; Bayat, A.; Yazdani, E.; Saievar-Iranizad, E. A comprehensive review on ultrasonic spray pyrolysis technique: Mechanism, main parameters and applications in condensed matter. *J. Anal. Appl. Pyrolysis* **2019**, *141*, 104631. [CrossRef]
45. Workie, A.B.; Ningsih, H.S.; Shih, S.-J. An comprehensive review on the spray pyrolysis technique: Historical context, operational factors, classifications, and product applications. *J. Anal. Appl. Pyrolysis* **2023**, *170*, 105915. [CrossRef]
46. Jamkhande, P.G.; Ghule, N.W.; Bamer, A.H.; Kalaskar, M.G. Metal nanoparticles synthesis: An overview on methods of preparation, advantages and disadvantages, and applications. *J. Drug Deliv. Sci. Technol.* **2019**, *53*, 101174. [CrossRef]
47. Shih, S.-J.; Chou, Y.-J.; Panjaitan, L.V.P. Synthesis and characterization of spray pyrolyzed mesoporous bioactive glass. *Ceram. Int.* **2013**, *39*, 8773–8779. [CrossRef]
48. Xia, W.; Chang, J. Well-ordered mesoporous bioactive glasses (MBG): A promising bioactive drug delivery system. *J. Control. Release* **2006**, *110*, 522–530. [CrossRef] [PubMed]
49. Shih, S.-J.; Lin, Y.-C.; Valentino Posma Panjaitan, L.; Rahayu Meyla Sari, D. The correlation of surfactant concentrations on the properties of mesoporous bioactive glass. *Materials* **2016**, *9*, 58. [CrossRef] [PubMed]
50. Youn, J.; Choi, J.H.; Lee, S.; Lee, S.W.; Moon, B.K.; Song, J.E.; Khang, G. Pluronic F-127/silk fibroin for enhanced mechanical property and sustained release drug for tissue engineering biomaterial. *Materials* **2021**, *14*, 1287. [CrossRef]

51. Mortazavi, S.; Rahsepar, M.; Hosseinzadeh, S. Modification of mesoporous structure of silver-doped bioactive glass with antibacterial properties for bone tissue applications. *Ceram. Int.* **2022**, *48*, 8276–8285. [CrossRef]
52. Chou, Y.-J.; Ningsih, H.S.; Shih, S.-J. Preparation, characterization and investigation of antibacterial silver-zinc co-doped β-tricalcium phosphate by spray pyrolysis. *Ceram. Int.* **2020**, *46*, 16708–16715. [CrossRef]
53. Shih, S.J.; Tzeng, W.L.; Jatnika, R.; Shih, C.J.; Borisenko, K.B. Control of Ag nanoparticle distribution influencing bioactive and antibacterial properties of Ag-doped mesoporous bioactive glass particles prepared by spray pyrolysis. *J. Biomed. Mater. Res. Part B Appl. Biomater.* **2015**, *103*, 899–907. [CrossRef]
54. Idalia, V.-M.N.; Bernardo, F. *Escherichia coli* as a model organism and its application in biotechnology. *Recent Adv. Physiol. Pathog. Biotechnol. Appl. Tech. Open Rij. Croat* **2017**, *13*, 253–274.
55. *ASTM E3031-15*; Standard Test Method for Determination of Antibacterial Activity on Ceramic Surfaces. ASTM international: West Conshohocken, PA, USA, 2015.
56. Kokubo, T.; Takadama, H. How useful is SBF in predicting in vivo bone bioactivity? *Biomaterials* **2006**, *27*, 2907–2915. [CrossRef] [PubMed]
57. Jung, O.; Smeets, R.; Hartjen, P.; Schnettler, R.; Feyerabend, F.; Klein, M.; Wegner, N.; Walther, F.; Stangier, D.; Henningsen, A. Improved in vitro test procedure for full assessment of the cytocompatibility of degradable magnesium based on ISO 10993-5/-12. *Int. J. Mol. Sci.* **2019**, *20*, 255. [CrossRef] [PubMed]
58. Miller, F.; Hinze, U.; Chichkov, B.; Leibold, W.; Lenarz, T.; Paasche, G. Validation of eGFP fluorescence intensity for testing in vitro cytotoxicity according to ISO 10993-5. *J. Biomed. Mater. Res. Part B Appl. Biomater.* **2017**, *105*, 715–722. [CrossRef]
59. Li, H.; He, W.; Pang, S.; Liaw, P.K.; Zhang, T. In vitro responses of bone-forming MC3T3-E1 pre-osteoblasts to biodegradable Mg-based bulk metallic glasses. *Mater. Sci. Eng. C* **2016**, *68*, 632–641. [CrossRef] [PubMed]
60. Gou, Z.; Chang, J. Synthesis and in vitro bioactivity of dicalcium silicate powders. *J. Eur. Ceram. Soc.* **2004**, *24*, 93–99. [CrossRef]
61. Ma, J.; Chen, C.; Wang, D.; Meng, X.; Shi, J. Influence of the sintering temperature on the structural feature and bioactivity of sol–gel derived SiO_2–CaO–P_2O_5 bioglass. *Ceram. Int.* **2010**, *36*, 1911–1916. [CrossRef]
62. Jones, J.R.; Ehrenfried, L.M.; Hench, L.L. Optimising bioactive glass scaffolds for bone tissue engineering. *Biomaterials* **2006**, *27*, 964–973. [CrossRef]
63. Sa, Y.; Guo, Y.; Feng, X.; Wang, M.; Li, P.; Gao, Y.; Yang, X.; Jiang, T. Are different crystallinity-index-calculating methods of hydroxyapatite efficient and consistent? *New J. Chem.* **2017**, *41*, 5723–5731. [CrossRef]
64. Workie, A.B.; Sefene, E.M. Ion-doped mesoporous bioactive glass: Preparation, characterization, and applications using the spray pyrolysis method. *RSC Adv.* **2022**, *12*, 1592–1603. [CrossRef]
65. Yang, Y.; Lu, C.; Yang, M.; Wang, D.; Peng, S.; Tian, Z.; Shuai, C. Copper-doped mesoporous bioactive glass endows magnesium-based scaffold with antibacterial activity and corrosion resistance. *Mater. Chem. Front.* **2021**, *5*, 7228–7240. [CrossRef]
66. Baino, F. Bioactive glasses–when glass science and technology meet regenerative medicine. *Ceram. Int.* **2018**, *44*, 14953–14966. [CrossRef]
67. Kumar, A.; Das, S.; Munusamy, P.; Self, W.; Baer, D.R.; Sayle, D.C.; Seal, S. Behavior of nanoceria in biologically-relevant environments. *Environ. Sci. Nano* **2014**, *1*, 516–532. [CrossRef]
68. Patil, S.N.; Paradeshi, J.S.; Chaudhari, P.B.; Mishra, S.J.; Chaudhari, B.L. Bio-therapeutic potential and cytotoxicity assessment of pectin-mediated synthesized nanostructured cerium oxide. *Appl. Biochem. Biotechnol.* **2016**, *180*, 638–654. [CrossRef] [PubMed]
69. Goh, Y.-F.; Alshemary, A.Z.; Akram, M.; Kadir, M.R.A.; Hussain, R. In-vitro characterization of antibacterial bioactive glass containing ceria. *Ceram. Int.* **2014**, *40*, 729–737. [CrossRef]
70. Youness, R.A.; Taha, M.A.; El-Kheshen, A.A.; El-Faramawy, N.; Ibrahim, M. In vitro bioactivity evaluation, antimicrobial behavior and mechanical properties of cerium-containing phosphate glasses. *Mater. Res. Express* **2019**, *6*, 075212. [CrossRef]
71. Garner, J.; Heppell, P. Cerium nitrate in the management of burns. *Burns* **2005**, *31*, 539–547. [CrossRef]
72. Cobrado, L.; Silva-Dias, A.; Azevedo, M.; Pina-Vaz, C.; Rodrigues, A. In vivo antibiofilm effect of cerium, chitosan and hamamelitannin against usual agents of catheter-related bloodstream infections. *J. Antimicrob. Chemother.* **2013**, *68*, 126–130. [CrossRef]
73. Aimei, C.; Qingshan, S.; Ouyang, Y.; Yiben, C. Effect of Ce^{3+} on membrane permeability of *Escherichia coli* cell. *J. Rare Earths* **2012**, *30*, 947–951.
74. Sobek, J.M.; Talburt, D.E. Effects of the rare earth cerium on *Escherichia coli*. *J. Bacteriol.* **1968**, *95*, 47–51. [CrossRef]
75. Thill, A.; Zeyons, O.; Spalla, O.; Chauvat, F.; Rose, J.; Auffan, M.; Flank, A.M. Cytotoxicity of CeO_2 nanoparticles for *Escherichia coli*. Physico-chemical insight of the cytotoxicity mechanism. *Environ. Sci. Technol.* **2006**, *40*, 6151–6156. [CrossRef]
76. Rodea-Palomares, I.; Boltes, K.; Fernández-Pinas, F.; Leganés, F.; García-Calvo, E.; Santiago, J.; Rosal, R. Physicochemical characterization and ecotoxicological assessment of CeO_2 nanoparticles using two aquatic microorganisms. *Toxicol. Sci.* **2011**, *119*, 135–145. [CrossRef] [PubMed]
77. Holtz, R.D.; Lima, B.A.; Souza Filho, A.G.; Brocchi, M.; Alves, O.L. Nanostructured silver vanadate as a promising antibacterial additive to water-based paints. *Nanomed. Nanotechnol. Biol. Med.* **2012**, *8*, 935–940. [CrossRef] [PubMed]
78. Eckhardt, S.; Brunetto, P.S.; Gagnon, J.; Priebe, M.; Giese, B.; Fromm, K.M. Nanobio silver: Its interactions with peptides and bacteria, and its uses in medicine. *Chem. Rev.* **2013**, *113*, 4708–4754. [CrossRef] [PubMed]
79. Xu, H.; Qu, F.; Xu, H.; Lai, W.; Andrew Wang, Y.; Aguilar, Z.P.; Wei, H. Role of reactive oxygen species in the antibacterial mechanism of silver nanoparticles on *Escherichia coli* O157: H7. *Biometals* **2012**, *25*, 45–53. [CrossRef]

80. Huang, Y.; Zhai, X.; Ma, T.; Zhang, M.; Pan, H.; Lu, W.W.; Zhao, X.; Sun, T.; Li, Y.; Shen, J. Rare earth-based materials for bone regeneration: Breakthroughs and advantages. *Coord. Chem. Rev.* **2022**, *450*, 214236. [CrossRef]
81. Kung, J.-C.; Chen, Y.-J.; Chiang, Y.-C.; Lee, C.-L.; Yang-Wang, Y.-T.; Hung, C.-C.; Shih, C.-J. Antibacterial activity of silver nanoparticle (AgNP) confined mesoporous structured bioactive powder against Enterococcus faecalis infecting root canal systems. *J. Non-Cryst. Solids* **2018**, *502*, 62–70. [CrossRef]
82. Atkinson, I.; Anghel, E.; Petrescu, S.; Seciu, A.; Stefan, L.; Mocioiu, O.; Predoana, L.; Voicescu, M.; Somacescu, S.; Culita, D. Cerium-containing mesoporous bioactive glasses: Material characterization, in vitro bioactivity, biocompatibility and cytotoxicity evaluation. *Microporous Mesoporous Mater.* **2019**, *276*, 76–88. [CrossRef]
83. Leonelli, C.; Lusvardi, G.; Malavasi, G.; Menabue, L.; Tonelli, M. Synthesis and characterization of cerium-doped glasses and in vitro evaluation of bioactivity. *J. Non-Cryst. Solids* **2003**, *316*, 198–216. [CrossRef]
84. Malavasi, G.; Lusvardi, G. Composition and morphology effects on catalase mimetic activity of potential bioactive glasses. *Ceram. Int.* **2020**, *46*, 25854–25864. [CrossRef]
85. Hench, L.L. Bioceramics: From concept to clinic. *J. Am. Ceram. Soc.* **1991**, *74*, 1487–1510. [CrossRef]
86. Vernè, E.; Di Nunzio, S.; Bosetti, M.; Appendino, P.; Brovarone, C.V.; Maina, G.; Cannas, M. Surface characterization of silver-doped bioactive glass. *Biomaterials* **2005**, *26*, 5111–5119. [CrossRef] [PubMed]
87. Lin, H.; Zhang, J.; Qu, F.; Jiang, J.; Jiang, P. In vitro hydroxyapatite-forming ability and antimicrobial properties of mesoporous bioactive glasses doped with Ti/Ag. *J. Nanomater.* **2013**, *2013*, 24. [CrossRef]
88. Chou, Y.-J.; Lin, S.-H.; Shih, C.-J.; Chang, S.L.; Shih, S.-J. The effect of Ag dopants on the bioactivity and antibacterial properties of one-step synthesized Ag-containing mesoporous bioactive glasses. *J. Nanosci. Nanotechnol.* **2016**, *16*, 10001–10007. [CrossRef]
89. El-Kady, A.M.; Ali, A.F.; Rizk, R.A.; Ahmed, M.M. Synthesis, characterization and microbiological response of silver doped bioactive glass nanoparticles. *Ceram. Int.* **2012**, *38*, 177–188. [CrossRef]
90. Shi, C.; Gao, J.; Wang, M.; Fu, J.; Wang, D.; Zhu, Y. Ultra-trace silver-doped hydroxyapatite with non-cytotoxicity and effective antibacterial activity. *Mater. Sci. Eng. C* **2015**, *55*, 497–505. [CrossRef]
91. Naseri, S.; Lepry, W.C.; Maisuria, V.B.; Tufenkji, N.; Nazhat, S.N. Development and characterization of silver-doped sol-gel-derived borate glasses with anti-bacterial activity. *J. Non-Cryst. Solids* **2019**, *505*, 438–446. [CrossRef]